Biomaterials 325 (2026) 123614

Contents lists available at ScienceDirect

Biomaterials

journal homepage: www.elsevier.com/locate/biomaterials

An antioxidative injectable chitosan hydrogel based on tannic acid modified dialdehyde polyurethane nano-crosslinker targeting RIPK1 to regulate neuroinflammation for amelioration of Parkinson's disease

Junpeng Xu [a,b,c,1], Chaohui Guo [c,1], Guangshuai Zhou [c,1], Haoman Chen [c,d,1], Peng Dai [c], Chonghui Tang [a], Shih-Ho Lin [e], Tsai-Yu Chen [e], Chen Zhang [f], Fanxuan Chen [d,g], Na Dong [c], Caiyan Li [c], Jie Pan [a], Xianzhen Chen [h], Ping Wu [c], Shengcun Li [i], Lihua Luo [f], Xiaokun Li [c,*], Jianwei Shuai [c,d,**], Shan-hui Hsu [e,***], Zhouguang Wang [b,c,****]

[a] Affiliated Cixi Hospital, Wenzhou Medical University, Ningbo, 315300, Zhejiang, China
[b] The First Affiliated Hospital of Wenzhou Medical University, Wenzhou, Zhejiang 325035, China
[c] Oujiang Laboratory (Zhejiang Lab for Regenerative Medicine, Vision and Brain Health), State Key Laboratory of Macromolecular Drugs and Large-scale Preparation, School of Pharmaceutical Science, Wenzhou Medical University, Wenzhou, 325000, Zhejiang, China
[d] Wenzhou Institute, University of Chinese Academy of Sciences, Wenzhou, 325000, Zhejiang, China
[e] Institute of Polymer Science and Engineering, National Taiwan University, Taipei, 106319, Taiwan, Republic of China
[f] School and Hospital of Stomatology, Wenzhou Medical University, Wenzhou, 324025, Zhejiang, China
[g] School of Biomedical Engineering, School of Ophthalmology and Optometry, Eye Hospital, Wenzhou Medical University, Wenzhou, 325000, China
[h] Department of Neurosurgery, Shanghai Tenth People's Hospital of Tongji University, Shanghai, 200072, China
[i] Rehabilitation Medicine Center, The Second Affiliated Hospital and Yuying Children's Hospital of Wenzhou Medical University, Wenzhou, 325000, Zhejiang, China

ARTICLE INFO

Keywords:
Chitosan hydrogel
Tannic acid
Polyurethane nano-crosslinker
Parkinson's disease
Neuroinflammation
RIPK1 signaling pathway

ABSTRACT

Parkinson's disease (PD) is one of the most common age-related neurodegenerative diseases. Currently, the treatment of PD is mainly based on surgery and medication, and there is a pressing necessity to develop a new generation of strategies incorporating biomaterials for treating PD. Herein, an antioxidative injectable chitosan hydrogel crosslinked with tannic acid-modified dialdehyde polyurethane nanoparticles (TA@DAP) to target RIPK1 is produced for ameliorating PD. The TA@DAP nano-crosslinker is newly synthesized via hydrogen bonding together with electrostatic interactions and is characterized by small angle X—ray with its data modeling, showing enhancement in dispersion stability, homogeneity, and bioactive capacity. The injectable hydrogel (CTDP) with sufficient modulus (~180 Pa) exhibits rapid self-healing (~7 min), shear-thinning injectability (30 gauge), and a uniform porous structure. In vitro, CTDP hydrogel significantly scavenges reactive oxygen species, promotes neural stem cell proliferation, and polarizes macrophages from pro-inflammatory M1 to anti-inflammatory M2 phenotypes. The CTDP hydrogel is injected into the brains of 6-hydroxydopamine-induced PD rats, demonstrating motor function restoration, dopaminergic neuron loss reduction, and suppression of neuroinflammation. Network pharmacology and molecular docking are employed to assist in screening for RIPK1-NF-κB-IκBα pathway as a key therapeutic mechanism. The bioactive injectable CTDP hydrogel provides a simple nanoparticle modification strategy integrated with advanced nanoscale characterization protocols while offering the possibility to explore the therapeutic mechanisms of composite biomaterials with network pharmacology and molecular docking, giving new concepts for the assessment of biomaterial preparations as well as for the treatment of PD.

* Corresponding author.
** Corresponding author. Oujiang Laboratory (Zhejiang Lab for Regenerative Medicine, Vision and Brain Health), State Key Laboratory of Macromolecular Drugs and Large-scale Preparation, School of Pharmaceutical Science, Wenzhou Medical University, Wenzhou, 325000, Zhejiang, China.
*** Corresponding author.
**** Corresponding author. The First Affiliated Hospital of Wenzhou Medical University, Wenzhou, Zhejiang 325035, China.
E-mail addresses: xiaokunli@wmu.edu.cn (X. Li), shuaijw@wiucas.ac.cn (J. Shuai), shhsu@ntu.edu.tw (S.-h. Hsu), wangzhouguang@wmu.edu.cn (Z. Wang).
[1] These authors contributed equally to this paper.

https://doi.org/10.1016/j.biomaterials.2025.123614
Received 27 May 2025; Received in revised form 21 July 2025; Accepted 7 August 2025
Available online 7 August 2025

1. Introduction

Parkinson's disease (PD) is a common age-related neurodegenerative disorder with progression and incurability [1]. The main pathological feature of PD is the loss of function in dopaminergic neurons (DAcNs) in the substantia nigra pars compacta (SNc) and dopaminergic fibers (DAcFs) in the striatum, as well as the projected brain region [1,2]. The behavioral abnormalities caused by PD, e.g., tremors and bradykinesia, primarily stem from irregular neuron firing in the subthalamic nucleus (STN) [3]. Meanwhile, DAcNs in the SNc are particularly susceptible to oxidative stress under hyperoxidative conditions, leading to neuroinflammation, which ultimately drives the progression of PD [4]. While there is no cure method for PD currently, clinical treatments like deep brain stimulation (DBS) or medication can generally alleviate the motor function symptoms for patients [5,6]. However, current clinical treatments have their limitations, such as risk of postoperative side effects and low treatment efficiency [7]. Precision medicine uses minimally invasive injection to accurately locate targeted drugs in the brain area, with a small drug loading dose and fast onset of action. Such a strategy requires the development of smart carriers like hydrogels [8].

Hydrogels are high water content polymeric networks formed through intermolecular or intramolecular interactions, characterized by high surface area and hydrophilicity [9–11]. Self-healing hydrogels as a popular category of smart hydrogel attract special interests because by mimicking the healing mechanisms inherent in living organisms [12]. Self-healing hydrogels prepared via dynamic Schiff linkages are preferred for biomedical engineering [13]. Chitosan with rich amine groups is a renewable polysaccharide as a promising polymer for the main chain of self-healing hydrogel [14,15]. Nevertheless, the main limitation of chitosan in biomedical applications is the poor water solubility. Carboxymethyl chitosan (CMC) improves the solubility and reactivity of chitosan without affecting the bioactivity, which is considered as an excellent candidate for preparing biomaterials in neural applications [16]. Moreover, chitosan-based hydrogels are usually soft and suffer durability issues [17]. Selecting proper crosslinker with good elasticity and biocompatibility can strengthen the chitosan network structure.

Functional crosslinkers can endow hydrogels with smart properties, for example dialdehyde polyurethane (DAP) nano-crosslinker, which was newly synthesized via a waterborne process to prepare self-healing hydrogels [18]. In addition, DAP possesses anti-inflammatory property, and the chemical structure of DAP can be adjusted to control the modulus and degradation rate of the hydrogel [19]. A recent study reported that a DAP-crosslinked conductive chitosan hydrogel, supplemented with gold nanoparticles to facilitate the gelling process, was synthesized as a bioactive hydrogel for treating PD [20]. However, DAP is dispersed in water through electrostatic interactions, which possibly leads to self-aggregation and further precipitation, and has a slow crosslinking rate because of the less exposed aldehyde groups. For PD treatment, scavenging reactive oxygen species (ROS) is a crucial design target of smart hydrogel, thus integrating DAP with natural polyphenolic molecules is a competitive strategy [21,22]. Tannic acid (TA) is a natural polyphenol-rich hydroxyl molecule with efficient ROS scavenging ability [23]. TA exerts neuroprotective effect on neurodegenerative diseases through multiple dimensions including anti-inflammatory property, antioxidant capacity, and modulation of cell signaling pathways [24–26]. Thus, these unique features make TA a promising candidate to prepare or modify biomaterials for treating neurodegenerative diseases as well as brain injuries.

Previous reports have shown that oxidized TA modified gold nanoparticles can serve as a conductive crosslinker to develop self-healing hydrogel to treat PD [27,28]. By integrating such polyphenolic compounds, DAP can be decorated through surface charge and hydrogen bonding interactions to possess extra smart properties. In the current study, a newly synthesized antioxidative nano-crosslinker, i.e., TA modified DAP (TA@DAP), was successfully developed and used to prepare an injectable bioactive self-healing hydrogel via dynamic Schiff linkages with CMC, as shown in Fig. 1. The hydrogel regulating neuroinflammation and autophagy showed stable crosslinking network, sufficient modulus, tiny needle injectability, and self-healing features. The bioactive hydrogel was found to enhance proliferation and scavenging ROS of neural stem cells (NSCs), together with polarizing macrophages from M1 to M2 phenotype. Furthermore, the potential therapeutic function of the hydrogel in PD treatment included promoting the motor function recovery and reducing the neurodegeneration of DAcNs and DAcFs via the precision hydrogel injection to the brain of PD-induced rats in vivo. Notably, network pharmacology and molecular docking identified receptor-interacting protein kinase 1 (RIPK1) as a core therapeutic target through database analysis, with TA exhibiting strong binding affinity to RIPK1. This interaction inhibits RIPK1-mediated necroptosis and nuclear factor kappa-B (NF-κB) activation, which are key pathways in PD-associated neurodegeneration. The efficacy of the hydrogel in downregulating RIPK1/NF-κB/inhibitor of NF-κB (IκBα) signaling in vivo was validated, which is correlated with reducing neuroinflammation and preserving neuronal integrity. By integrating computational insights with material design, this work establishes a multifunctional therapeutic strategy targeting oxidative stress and RIPK1-driven inflammation, advancing precision biomaterials for neurodegenerative disorders.

2. Materials and methods

2.1. Synthesis and characterization of tannic acid modified dialdehyde polyurethane (TA@DAP) nano-crosslinker

DAP has been synthesized via a waterborne process in our previous study [18]. Poly(ε-caprolactone) diol (PCL diol; 189421, Mn = ~2000 Da; Sigma-Aldrich, USA) and isophorone diisocyanate (IPDI; 42760, 98+%, Acros Organics, USA) were combined in a 5:2 mass ratio and allowed to react at 75 °C for 3 h under nitrogen protection, utilizing 0.05 % tin(II) 2-ethylhexanoate (B23612, 95 %, Alfa Aesar, USA) as a catalyst. Subsequently, 2,2-bis(hydroxymethyl)propionic acid (DMPA; 106615, 98 %, Sigma-Aldrich, USA) as a chain extender and methyl ethyl ketone (BAKR8052.2500, >99 %, J.T. Baker, USA) were introduced into the reflux apparatus for an additional hour of reaction. The carboxylic acid groups were then neutralized through treatment with triethylamine (TEA; JT91117, ≥99.5 %, J.T. Baker, USA) at 50 °C for 30 min. Deionized water (DI water; resistivity = 18.2 MΩ cm) was incorporated into the system under vigorous mechanical agitation, followed by the addition of ethylenediamine (EDA; ER0527-002, 99 %, Tedia, USA) for a subsequent 1-h reaction period. The terminal urethane groups were ultimately functionalized with glyoxal (A16144, 40 % w/w aq. soln., Alfa Aesar, USA) to yield aldehyde-modified polyurethane, i.e., DAP. The molar stoichiometry of PCL diol:DMPA:IPDI:EDA:TEA:glyoxal was precisely maintained at 1:1:2.7:0.7:1:0.7 throughout the synthesis.

TA@DAP was newly prepared as a secondary modification after DAP successful synthesis. After removal of excess organic solvent by depressurized distillation, concentrations of TA (403040, ACS reagent grade, Sigma-Aldrich, USA) solution, varying from 15 to 31.25 μg/mL, were added dropwise to the DAP dispersion under vortex shaking to produce homogeneous TA@DAP nano-crosslinker dispersion, and the maximum concentration of TA modification was determined by the presence of precipitation.

2.2. Morphology and structure characterization using small-angle X-ray scattering (SAXS)

The synthesis of TA@DAP was characterized by Fourier transform infrared spectroscopy (IR; Nicolet is50; Thermo Fisher, USA) with a wavenumber range from 4000 to 1000 cm^{-1}. The ζ-potentials and average hydrodynamic diameters (R_h) were validated by a multifunction nanoparticle analyzer (Zetasizer ultra; Malvern panalytical, UK). The

morphological and nanostructural differences with DAP were demonstrated by transmission electron microscopy (TEM, Talos F200S G2; FEI, USA) and small-angle X-ray scattering (SAXS) together with their model-fitting data.

The coherent SAXS experiments were performed at beamline station 25A1 of the Taiwan Photon Source (TPS 25A1) located at the National Synchrotron Radiation Research Center (NSRRC) in Hsinchu, Taiwan [29]. The incident photon energy was calibrated to 8.83 keV, with a calibrated sample-to-detector distance of 6 m, yielding a measurable q-range spanning from 0.014 to 1.4 nm^{-1}. The momentum transfer vector (q) was determined using Equation (1):

$$q = 4\pi \frac{sin\frac{\theta}{2}}{\lambda} \quad \text{Equation 1}$$

where θ is the scattering angle and λ is the wavelength of X-ray. The exposure duration was maintained at 2 s, with each data curve representing an average of ten consecutive measurement repetitions. The incident beam was collimated to a 10 μm^2 cross-sectional area, and coherent scattering patterns were acquired using a photon detection system (PI-LCX, Princeton Instruments, USA) equipped with a charge-coupled device sensor.

The coherent SAXS curves were modeled using the SasView software (4.2.2 version). The following model function (Equation (2)) was used to fit the scattering curves from coherent SAXS experiments:

$$I(q) = I_0 P_{HS}(q) S_{HS}(q) + I_{OZ}(q) + I_{bkg} \quad \text{Equation 2}$$

where $I(q)$ indicates the overall intensity after data reduction from the experiment and I_0 is the scaling factor. I_{bkg} denotes the background.

$P_{HS}(q)$ is the hard sphere form factor for a monodisperse spherical particle, defined by Equation (3) [30]:

$$P_{HS}(q) = \frac{scale}{V_{HS}} \times \left[\frac{3V(\Delta\rho)\left(\sin(qR_{np}) - qR_{np}\cos(qR_{np})\right)}{(qR_{np})^3}\right]^2 \quad \text{Equation 3}$$

where *scale* is a volume fraction, V_{HS} calculated by $V = 4\pi r^3/3$ represents the volume of hard sphere, R_{np} is the radius of the sphere, and the scattering length density (Sld, ρ) of water, i.e., $\rho = 9.46 \times 10^{-6}$ Å^{-2}.

$S_{HS}(q)$ is the hard-sphere structure factor using the Percus-Yevick approximation to model (Equation (4)) the correlation between the particles [31]:

$$S_{HS}(q) = \frac{1}{1 + 24\eta G(2R_{HS}q)/2R_{HS}q} \quad \text{Equation 4}$$

where R_{HS} is the hard-sphere radius which denotes as a half of the center-to-center distance between the particles. η is the hard-sphere volume fraction that shows the correlating fraction of particles.

Finally, $I_{OZ}(q)$ denotes the Ornstein-Zernike equation (Equation (5)) [32], describing the average localized chain distances between chain segments within nanospheres

$$I_{OZ} = \frac{I'_{scale}}{1 + (\xi q)^2} \quad \text{Equation 5}$$

where ξ is the correlation length of concentration fluctuations and I'_{scale} is the scaling factor. These fluctuations give rise to the scattering at the high-q region.

Guinier equation (Equation (6)) was employed to characterize the radius of gyration (R_g), and the shape factor was further defined as Equation (7).

$$ln[I(q)] = -\frac{q^2 R_g^2}{3} + ln[I(0)] \quad \text{Equation 6}$$

$$shape\ factor = \frac{R_g}{R_h} \quad \text{Equation 7}$$

for fitting in the Guinier region, the q in a limited range, $q\text{-}min < q < 1.3\ R_g^{-1}$, was used.

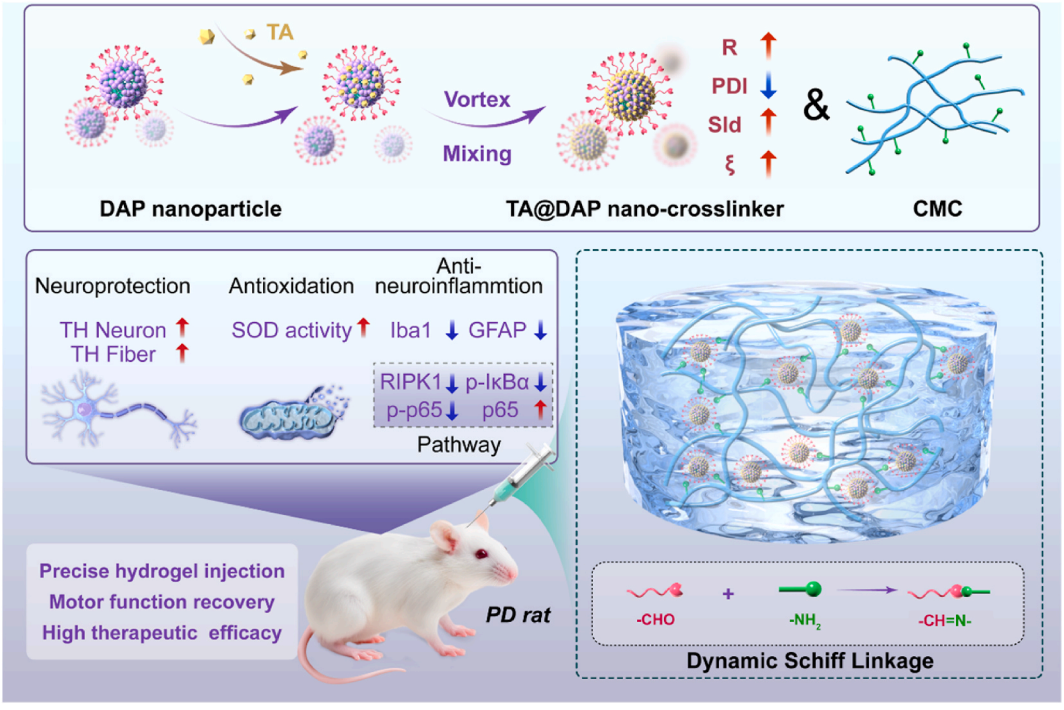

Fig. 1. Illustration of the preparation for a tannic acid (TA)-modified dialdehyde polyurethane (DAP) nano-crosslinker (TA@DAP) and a bioactive self-healing chitosan hydrogel crosslinked with TA@DAP possessing the capabilities of neuroprotection and antioxidation, as well as targeting RIPK1 via NF-κB p65-IκBα pathway for regulating the neuroinflammation to achieve multi-dimensional treatment of Parkinson's disease (PD). R: redius; PDI: polydiversity; Sld: scattering length density; ξ: correlation length; CMC: carboxymethyl chitosan; TH: tyrosine hydroxylase; SOD: superoxide dismutase.

2.3. Preparation, physicochemical properties, and rheological analysis of CMC/TA@DAP (CTDP) hydrogel

The injectable hydrogel, i.e., CTDP hydrogel, is produced from CMC (Mw~300,000, Biosynth-carbosynth, UK) as the main chain crosslinked by TA@DAP nano-crosslinker. The crosslinking of CTDP hydrogels is mainly formed by dynamic Schiff base linkages supplemented by hydrogen bonding, with a mixture of two solutions available for gelation at room temperature. The optimization of the gel control group, namely CDP hydrogel composed of 2 wt% CMC and 2 wt% DAP, in this study has been discussed in detail in previous studies [20]. While considering the biocompatibility of CTDP hydrogels, the maximum concentration of TA acceptable to the cells was determined as an important parameter for the optimization of CTDP hydrogel preparation.

The internal cross-sectional porous structure of CTDP hydrogels was visualized by field emission scanning electron microscopy (SEM; SU8010, HITACHI, Japan). The in vitro degradation of hydrogels was estimated by tracking the residual mass over time. Hydrogels soaked at a constant temperature of 37 °C were removed from saline at the specified time points, rinsed with deionized water, and then freeze-dried. The percentage of residual weight was calculated by Equation (8):

$$\textit{weight remain}\ (\%) = \frac{W_0}{W} \times 100\% \qquad \text{Equation 8}$$

where W_0 is the initial dry weight of the hydrogel and W is the dry weight of the hydrogel after removal at the specified time.

The rheological characteristics of the CTDP hydrogels were evaluated at 25 °C using a rheometer (DHR-2, TA Instruments, USA) equipped with a cone and plate geometry featuring a diameter of 40 mm and a cone angle of 2°. Measurements of the storage modulus (G') and loss modulus (G") were conducted at a frequency of 1 Hz and a dynamic strain of 1 % as a function of the gelling time. Dynamic strain sweep experiments on the hydrogels were performed at a frequency of 1 Hz within the dynamic strain amplitude range of 200 %–800 %. The self-healing properties of the equilibrium hydrogels were examined through rheological experiments, in which continuous and alternating high strain (700 %) and low strain (1 %) conditions were applied as damage-healing cycles at a frequency of 1 Hz. The steady shear test was employed to characterize the shear-thinning behavior of the CTDP hydrogel. This behavior was determined by measuring the viscosity in relation to the shear rate. The free radical scavenging capacity of saline (CN; negative control), DAP, TA@DAP, CDP gel, CTDP gel, and vitamin C (VC; positive control) was evaluated using 2,2-diphenyl-1-picrylhydrazyl (DPPH; Aladdin, China). Absorbance measurements were conducted at 517 nm using a UV–vis spectrometer (Evolution 350, Thermo Fisher Scientific, USA) to quantify the differential scavenging activity among the groups. The assay compared the ability of each sample to neutralize DPPH radicals, with VC serving as a reference standard for antioxidant efficacy.

2.4. Cell culture and in vitro cell experiments

The NE-4C cells (RRID: CVCL_B063), which is one of NSC cell lines and originally obtained from American Type Culture Collection (ATCC), were procured from Wuhan Sunncell Biotechnology Co., Ltd. (Wuhan, China). Cells were cultured and maintained in Eagle's Minimum Essential Medium (EMEM; Gibco, USA) supplemented with 10 % fetal bovine serum (FBS; Sigma-Aldrich, USA) and 1 % penicillin-streptomycin antibiotics (PS; Gibco, USA) under standard conditions. The cytotoxicity within 24 h of the maximum TA concentration in cell culture and the proliferative effects of hydrogels within 3 days were evaluated using the Cell Counting Kit-8 (CCK-8; New Cell & Molecular Biotech., China). Absorbance measurements were conducted at 450 nm with a microplate reader (Multiskan SkyHigh 1550; Thermo Fisher Scientific, USA). Cell viability for all hydrogel groups was normalized to the control group, defined as cells cultured in medium alone.

The superoxide dismutase (SOD) activity variations in lipopolysaccharide (LPS)-induced NE-4C cells were assessed using a Total Superoxide Dismutase Assay Kit with WST-8 (Beyotime Biotech., China) following the manufacturer's protocol. Absorbance measurements were recorded at 450 nm using the microplate reader. The reactive oxygen species (ROS) scavenging capacity was evaluated using a ROS Assay Kit (Beyotime Biotechnology, Shanghai, China). Following 24 h of LPS-induced inflammation (1 mg/mL; Sigma-Aldrich, USA) in NE-4C cells, hydrogel groups were co-cultured with LPS-stimulated NE-4C cells operated with Transwell chamber (Costar, USA) for 24 h. Cells were stained with 10 μM 2′,7′-dichlorodihydrofluorescein diacetate (DCFH-DA; Beyotime Biotech., China), a ROS-sensitive fluorescent probe, at 37 °C for 20 min, and fluorescence images were acquired via an inverted fluorescence microscope (Axio Observer 7; ZEISS, Germany). Healthy (negative control) and LPS-treated (positive control) NE-4C cells served as experimental baselines. Quantitative analysis of fluorescence intensity was performed using ImageJ software.

The BV2 mouse microglial cell line (RRID: CVCL_C8UX) was acquired from the Chinese Academy of Sciences Cell Bank (Shanghai, China) and maintained in high-glucose Dulbecco's Modified Eagle's Medium (DMEM; Gibco, USA) supplemented with 10 % FBS and 1 % PS for routine cell propagation. For inflammation experiments, BV2 cells were cultured in PS-free DMEM containing 10 % FBS to eliminate potential antibiotic interference. The in vitro microglia polarization assay was conducted by first inducing M1 polarization in BV2 cells through treatment with LPS (1 mg/mL) for 12 h. Following polarization, experimental groups—including a control (unpolarized cells), only LPS-induced (untreated) cells, DAP-treated (1 wt% in 200 μL), TA@DAP-treated (1 wt% in 200 μL), CDP hydrogel (200 μL), and CTDP hydrogel (200 μL)—were added to 24-well plates pre-seeded with BV2 cells and co-cultured for an additional 12 h.

The protein expression levels of NSCs were further investigated by immunofluorescence staining (IF) and Western blot (WB) analyses. BV2 cells growing on the glass slides were fixed by 4 wt% paraformaldehyde (PFA, Sigma-Aldrich, USA) for 15 min at room temperature after removing medium and washed by 0.1 wt% Tween 20 in PBS (PBST) three times. BV2 cells were blocked in a 2 wt% bovine serum albumin (BSA, Gibco, USA) solution (diluted with PBST) for 1 h with shaking at the speed of 60 rpm. Then, BV2 cells were incubated with anti-IL-1β antibody (1:200, AF5103; Affinity, UK) or anti-CD206 antibody (1:200, DF4149; Affinity, UK) at 4 °C overnight. On the next day, cell-loaded slides were washed by PBST and incubated with CoraLite488-conjugated Goat Anti-Rabbit IgG(H + L) (1:200, SA00013-2; Proteintech, China), or Dylight594, Goat Anti-Rabbit IgG(H + L) (1:200, E032420-01; EARTH, China) for 1 h at 25 °C. The cells nuclei were counterstained with the DAPI Staining Solution (Beyotime Biotech., China). The photomicrographs were captured with a Multispectral fast laser confocal microscope (FV3000, Olympus Evident, Japan). The semi-quantitative data for average fluorescent intensity of IL-1β- and CD206-positive BV2 cells were calculated and acquired using ImageJ software.

The WB method was further employed to quantitate the protein expression levels. The cell lysates were vortexed intermittently every 10 min for 1 h at 4 °C, mechanically homogenized by repeated pipetting, and centrifuged at 12,000×g for 10 min at 4 °C. The supernatant was collected, and protein concentration was determined using a Bicinchoninic Acid (BCA) Protein Assay Kit (WB6501; New Cell & Molecular Biotech., China) according to the manufacturer's protocol. Samples containing 40 μg of total protein per lane were resolved on a 15 % sodium dodecyl sulfate-polyacrylamide gel electrophoresis and transferred onto a 0.45 μm polyvinylidene fluoride membrane (PVDF Immobilon-P, IPVH00010; Millipore, USA). Membranes were blocked with 5 % (w/v) skimmed milk in TBST for 2 h at room temperature. Primary antibodies included anti-IL-1β (1:1000, ~31 kDa, AF5103; Affinity Biosciences, UK), anti-CD206 (1:1000, ~260 kDa, DF4149; Affinity Biosciences, UK), anti-TNF-α (1:1000, ~17 kDa, AF7014; Affinity

Biosciences, UK), anti-iNOS (1:1000, ~130 kDa, AF1099; Affinity Biosciences, UK), and anti-β-actin (1:5000, ~42 kDa, AF7018; Affinity Biosciences, UK). Membranes were incubated overnight at 4 °C, washed three times with TBST, and probed with HRP-conjugated Goat Anti-Rabbit IgG (H + L) secondary antibody (1:1000, A0208; Beyotime Biotech., China) in 5 % skimmed milk for 2 h at room temperature. Protein bands were imaged with a ChemiDoc XRS + Imaging System (Bio-Rad, USA). Band intensities were quantified using ImageJ software.

2.5. Rat model of Parkinson's disease (PD) and in-situ stereotaxic injection

Male Sprague Dawley (SD) rats (200–220 g body weight) were procured from Beijing Vital River Laboratory Animal Technology Co., Ltd. (Beijing, China). All experimental protocols were approved by the Institutional Animal Care and Use Committee (IACUC) of Oujiang Laboratory (Approval No. OJLAB24122503) and conducted in accordance with the National Institutes of Health (NIH) Guide for the Care and Use of Laboratory Animals. Animals were housed under controlled environmental conditions with a 12-h light/dark cycle and provided ad libitum access to food and water.

A validated PD model was established via unilateral stereotaxic injection of 6-hydroxydopamine (6-OHDA; Sigma-Aldrich, USA) into the medial forebrain bundle (mfb), as previously described [33,34]. Previous work has reported that in situ injections can be performed with either the striatum or the mfb [20,35]. The selection of the mfb as the target brain region is due to its intermediate position between the striatum and the SNc regulatory axis, which allows for better efficacy. Briefly, rats were anesthetized with Zoletil™ 50 (40 mg/kg, Virbac, France), and 6-OHDA (2 μg/μL in 0.02 wt% ascorbic acid saline solution, 4 μL each) was delivered into the mfb (AP −2.8 mm, ML −2.0 mm, DV −8.0 mm relative to bregma, refer to Paxinos and Watson's Rat Brain Mapping Coordination [36]) via a 26-gauge Hamilton microsyringe (702RN-25μl; Hamilton Company, USA) for a rate of 0.5 μL/min using a stereotactic frame (ZH-Lanxing C/S; Zhenghua Biologic Apparatus Facilities Co., Ltd, China) coupled with a micro syringe pump system (ZH-KES; Zhenghua Biologic Apparatus Facilities Co., Ltd, China). Postoperative analgesia (e.g., buprenorphine) and monitoring were performed to ensure animal welfare. To minimize reflux along the injection tract, the cannula was retained in situ for an additional 5 min following 6-OHDA administration. Lesion efficacy was evaluated by quantifying apomorphine (APO)-induced rotational behavior. APO (Sigma-Aldrich, USA) was administered subcutaneously (0.05 mg/kg) as a 5 mg/mL solution in 0.2 % (w/v) ascorbic acid-saline. Rats exhibiting >25 contralateral rotations per 5 min interval, consistently directed toward the side opposite the lesion, were deemed to have successful unilateral nigrostriatal pathway destruction and included in subsequent PD model analyses [33,37].

Rats with validated PD induction were selected for unilateral intrastriatal administration of saline or treatment group, i.e., DAP, TA@DAP, CDP hydrogel, and CTDP hydrogel. Under anesthesia with injection of Zoletil™ 50, animals were secured in the stereotaxic frame. Using coordinates corresponding to the prior 6-OHDA lesion site, 4 μL of target solution or hydrogel was infused via a 26-gauge Hamilton microsyringe at a rate of 0.5 μL/min. The needle remained in situ for 5 min post-injection to minimize reflux, followed by gradual withdrawal. Each experimental group comprised $n \geq 6$ rats for longitudinal assessments, including behavioral tests, electrophysiological analysis, immunofluorescent staining, and WB quantifications. A sham-control group (healthy rats receiving saline instead of 6-OHDA during initial surgery) was included to establish baseline neurobehavioral and histological parameters.

2.6. Behavioral tests and electrophysiological analysis of PD rats

Rotational behavior was assessed at 7 and 14 days post-treatment via subcutaneous administration of APO. Rats were placed in a circular open-field arena (diameter: 60 cm), and full contralateral rotations (360° turns toward the lesion side) were recorded for 5 min. Rotational velocity (turns/min) was calculated to quantify the attenuation of PD-related motor asymmetry. Forelimb lateralization was evaluated using the cylinder test, which exploits the innate exploratory behavior of rodents in novel environments. Rats were individually placed in a transparent glass cylinder (22 cm diameter × 26 cm height) under dim lighting, and forelimb contacts with the cylinder wall were recorded for 5 min. The percentage of ipsilateral (impaired) and contralateral (unimpaired) forelimb contacts relative to the total contacts was calculated and compared to age-matched healthy controls.

The electrophysiological analysis was conducted by following literature with some modifications [27,34]. Rats were anesthetized with Zoletil™ 50 and secured in the stereotaxic frame. A craniotomy was performed to expose the subthalamic nucleus (STN), followed by careful removal of the dura mater to enable microelectrode access. Extracellular neuronal activity was recorded using an 8-channel microelectrode array (Kedou Biotech., China) positioned stereotaxically within the STN (coordinates relative to bregma: AP −3.8 mm, LAT −2.4 mm, DEP −6.5 mm) [38]. Signals were amplified via a differential AC preamplifier (Model 3600; A-M Systems, USA) with a bandpass filter and digitized at 25 kHz using a data acquisition interface (Power1401-3A; Cambridge Electronic Design, UK). Raw signals were monitored in real-time on a digital oscilloscope (TPS2014; Tektronix, USA) and stored for offline analysis. Neuronal spikes with a signal-to-noise ratio≥3:1 were isolated using amplitude thresholding. Spontaneous firing rates were quantified from 30-s continuous recordings during quiet wakefulness. Spike sorting and rate calculations were performed using Spike2 software (v8.21; Cambridge Electronic Design), with interspike interval histograms generated to assess firing regularity.

2.7. Histological staining, ex vivo imaging, WB, nitric oxide (NO) levels, and SOD activity for brain tissue

Immunofluorescent staining was performed to evaluate in vivo biocompatibility and histological markers of PD. Tissue sections were incubated overnight at 4 °C with primary antibodies: anti-tyrosine hydroxylase (TH) rabbit polyclonal antibody (1:300, GB11181; Servicebio, China) to assess dopaminergic neuron/fiber integrity, anti-Iba1 mouse monoclonal antibody (1:500, GB12105; Servicebio, China) to quantify microglial activation, and anti-glial fibrillary acidic protein (GFAP) rabbit polyclonal antibody (1:1000, GB111096; Servicebio, China) to evaluate astrocyte reactivity. After rinsing, sections were incubated for 1 h at 25 °C with species-specific secondary antibodies: Cy3-conjugated goat anti-rabbit IgG (1:300, GB21303; Servicebio, China), Cy3-conjugated goat anti-mouse IgG (1:300, GB21301, Servicebio, China), and Alexa Fluor 488-conjugated goat anti-rabbit IgG (1:400, GB25303; Servicebio, China). Fluorescence micrographs were acquired using a digital slide scanner (Pannoramic MIDI, 3DHISTECH Ltd., Hungary), and mean fluorescence intensity was quantified across anatomically defined regions of interest using ImageJ software, with background signal normalized to negative controls. As for hematoxylin and eosin (H&E) staining (standard type; Jiangsu KeyGen Biotech Co., Ltd., Nanjing, Jiangsu Province, China), the staining was operated according to the manufacturer's instructions only for the group of CTDP hydrogel-treated PD rats. The H&E-stained sections were visualized under an optical microscopy (Olympus, Tokyo, Japan). As for ex vivo imaging, fluorescein 5-isothiocyanate (FITC; MedChemExpress, USA) was utilized as a fluorescent label and bonded with the TA@DAP for further in vivo tracing. The ex vivo imaging was performed only for the CTDP hydrogel-treated group. The rat brains were harvested at 3, 7, and 14 days and the fluorescence imaging was visualized via a NEWTON 7.0 Imaging System (Vilber, France).

Extracted brain tissue was homogenized in a modified radioimmunoprecipitation buffer supplemented with a 10 μL/mL protease

inhibitor mixture. Homogenates were centrifuged at 12,000×*g* for 15 min at 4 °C, and supernatants were collected for total protein quantification using the BCA assay. WB procedures followed the protocol outlined in Section 2.4 for in vitro experiments. Membranes were probed with the following primary antibodies: anti-β-actin (~42 kDa, 1:5000, AF7018; Affinity Biosciences, UK), AFfirm™ anti-α-synuclein (~18 kDa, 1:1000, BF8041; Affinity Biosciences, UK), anti-RIPK1 (~76 kDa, 1:2000, AF7877; Affinity Biosciences, UK), anti–NF–κB p65 (~60 kDa, 1:2000, AF5006; Affinity Biosciences, UK), anti-phospho–NF–κB p65 (~60 kDa, Ser536; 1:2000, AF2006; Affinity Biosciences, UK), anti-IκBα (~36 kDa, 1:2000, AF5002; Affinity Biosciences, UK), anti-phospho-IκBα (~36 kDa, Ser32; 1:2000, AF2002; Affinity Biosciences, UK), anti-Cleaved-Caspase 3 (~17 kDa, Asp175; 1:1500, AF7022; Affinity Biosciences, UK), anti-Bax (~21 kDa; 1:2000, AF0120; Affinity Biosciences, UK), and anti-Bcl-2 (~26 kDa; 1:2000, AF6139; Affinity Biosciences, UK). HRP-conjugated secondary antibodies included goat anti-rabbit IgG (H + L) (1:5000, A0208; Beyotime Biotech., China) and goat anti-mouse IgG (H + L) (1:5000, A0216; Beyotime Biotech., China). Protein bands were visualized using the ChemiDoc XRS + Imaging System and quantified via ImageJ software, with β-actin serving as a loading control for normalization.

Nitric oxide (NO) levels were quantified colorimetrically using a Total Nitric Oxide Assay Kit (S0024, Beyotime Biotech., China) based on the Griess reaction, which detects total nitrate/nitrite concentrations. Absorbance at 540 nm was measured spectrophotometrically with the microplate reader, and NO concentrations were interpolated from a sodium nitrite standard curve (0–100 μM) generated using GraphPad Prism 10.1.2. SOD activity in the targeted brain region was assessed using the assay kit, as previously described in Section 2.4. Data were normalized to tissue weight (mg) to account for regional variations in protein content.

2.8. Network pharmacology and molecular docking

The pharmacologically active components of CTDP hydrogel (CMC, TA, polyurethane) were mapped to human gene targets via UniProt, while PD-associated genes were systematically curated from OMIM and GeneCards. Redundant entries across databases were consolidated and removed using Excel (Microsoft, USA), yielding a final list of PD-related target genes. EVenn intersection analysis identified shared targets subsequently incorporated into a Cytoscape-constructed PPI network [39]. STRING database interrogation (Homo sapiens, interaction score >0.9) revealed RIPK1 as the paramount therapeutic target through topological analysis of centrality metrics. DAVID bioinformatics analysis confirmed significant pathway enrichment ($p < 0.05$) in PD-related neuroinflammatory and neuronal survival mechanisms.

The 2D structures of small-molecule ligands were obtained from the PubChem database (http://pubchem.ncbi.nlm.nih.gov/) and converted into 3D structures using ChemOffice 20.0 software [40]. These structures were then saved in mol2 format. High-resolution crystal structures of protein targets were selected from the RCSB PDB database (http://www.rcsb.org/) as molecular docking receptors. Protein preparation, including the removal of water molecules and phosphate groups, was performed using PyMOL 2.6.0, and the processed structures were saved in PDB format. The Molecular Operating Environment (MOE) 2019 software was used to perform energy minimization of the compounds, preprocess the target proteins, and identify active binding pockets. Molecular docking was carried out using MOE 2019, with the number of docking runs set to 50. The binding affinity was evaluated based on the calculated binding energy, and the results were visualized using PyMOL 2.6.0 and MOE 2019 for further analysis.

2.9. Statistical analysis

All experiments were performed with $n \geq 3$ biological replicates, and quantitative data were derived from independently repeated trials. Results are expressed as mean ± standard deviation (SD). For comparisons across multiple groups, statistical significance was assessed using one-way analysis of variance (ANOVA) followed by Tukey's post-hoc test ($\alpha = 0.05$). Behavioral data, collected at multiple time points within the same cohort, were analyzed via two-way repeated-measures ANOVA to account for time- and treatment-dependent effects, with Tukey's post-hoc test applied for pairwise comparisons. Statistical computations were performed using GraphPad Prism 10.1.2. A threshold of $p < 0.05$ (indicated by asterisks in figures) was considered statistically significant.

3. Results and discussion

3.1. Synthesis and characterization of TA@DAP

The DAP was synthesized following the previous reported work [18,20], and the TA modified DAP nano-crosslinker, i.e., TA@DAP, was further produced via synthetic routes demonstrated in Fig. 2A. TA has been attempted as a modifier molecule in many types of nanoparticles because of its antioxidant and hydrophilic properties as well as possessing rich active hydrogen bonding [41]. The IR spectra of TA, DAP, and TA@DAP are demonstrated in Fig. 2B, which verified the existence of strong hydroxyl groups and carbonyl groups in TA@DAP. For the pristine TA, the absorption bands in the wavenumber range 3000–3700 cm^{-1} and near 1613 cm^{-1} were ascribed to the vibration of the phenolic hydroxyl groups. The stretching vibration of C═O resonance and on the aromatic rings of TA showed up at 1716 and 1203 cm^{-1}, respectively. In DAP, the specific characterized peaks of aldehyde groups included the contribution from C–H bending, asymmetric C–H stretching, and N–H stretching at 1366 cm^{-1}, 2949 cm^{-1} (coupled with 2867 cm^{-1}), and 3366 cm^{-1}, respectively. Both the characteristic peaks of TA and DAP were clearly detected in the newly prepared TA@DAP, suggesting the successful synthesis of TA modified DAP nano-crosslinker. Also, the carbonyl group peak in TA@DAP showed a significant redshift as well as large intensity decrease from the strong hydrogen-bonded carbonyl peak in TA, possibly implying that the phenolic hydroxyl group in TA may exist in hydrogen bonding with the carbonyl group in DAP [42]. The results of IR can generally infer that TA@DAP is in the form of complex nanoparticles. The largest amount of TA available to modify DAP is demonstrated by photo images in Fig. S1. The maximal concentration of TA that can mix with 8 wt% DAP dispersion was confirmed to be < 26.25 mg/mL in the case of ensuring the stability of TA@DAP. Meanwhile, the highest concentration of TA achievable for NE-4C cells to have a high level of viability (over 80 % tested by CCK8) was 5 mg/mL, shown in Fig. S2, which is consistent with other related works [25,43]. Base on the above-mentioned optimization process and the concentration change after hydrogel preparation, TA at 20 mg/mL mixed with DAP at 8 wt% under vortex oscillation condition was finally selected to prepare TA@DAP nanoparticle suspension.

The topography of DAP and TA@DAP nano-crosslinkers are illustrated in the TEM images of Fig. 2C and D, respectively. The morphology of DAP after negative staining was observed to be consistent with the previous report (~20 nm), showing polymeric nanospherical structures with a relatively low particle uniformity [18]. The spherical-like TA@DAP nanoparticles (~25 nm) with higher homogeneity were also clearly seen and exhibited markedly different opaque sphere structures under the view of TEM. Also, the zeta potential and hydrodynamic diameter (two times of R_h) of nanoparticles were obtained using multifunction nanoparticle analyzer. DAP and TA@DAP synthesized in this research both showed adequate surface electronegativity, i.e., −39.5 ± 0.51 mV and −43.2 ± 0.35 mV, respectively, which represents better dispersion of TA-modified nanoparticles in an aquatic environment [44]. The average hydrodynamic diameters of DAP and TA@DAP were 23.8 ± 0.98 and 28.6 ± 0.70 nm, respectively. The histograms of the two nanoparticle sizes are presented in Fig. S3, clearly showing that TA@DAP has a narrower distribution of particle size than DAP.

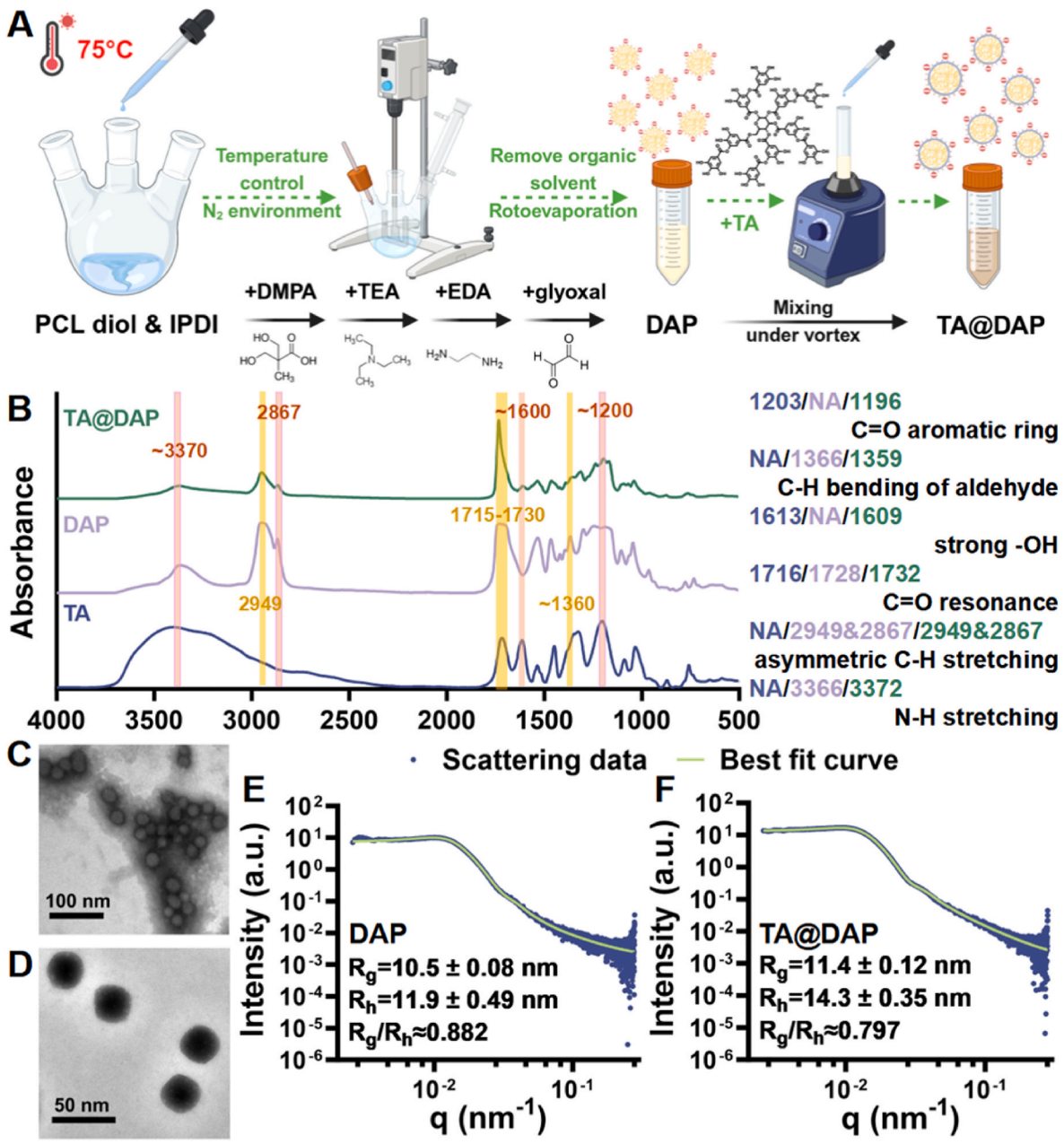

Fig. 2. Preparation and characterization of TA@DAP nano-crosslinker. (A) The synthetic diagram of DAP and TA@DAP nano-crosslinkers. Images created with BioRender.com. (B) The IR spectra of TA, DAP, and TA@DAP. (C) The TEM image of DAP. (D) The TEM image of TA@DAP. The SAXS profiles for (E) DAP and (F) TA@DAP nanoparticles with matching best fitting curves.

The nanostructures of DAP and TA@DAP were analyzed in detail using coherent SAXS, demonstrated in Fig. 2E and F [45]. Based on the characteristics of DAP polymer nanoparticles, the monodisperse hard-sphere model is used as the main model, and the OZ model is supplemented with the simulation of chain segment changes inside the sphere to interpret the SAXS data. The SAXS profiles of both DAP and TA@DAP nanoparticles showed very clear spherical particle form factors. The fitting model (Equation (2)) included hard sphere form and structure factors to describe nanoparticles and their correlation, together with the Ornstein-Zernike equation to describe the local concentration fluctuations [46,47]. All resulted fitting parameters are listed in Table 1. After TA modification, the sphere radius (R_{np}) increased from 12.40 ± 0.11 nm to 13.62 ± 0.07 nm, together with more homogeneous particle polydispersity (PDI; 0.28 *vs* 0.23). The fitted particle sizes remain largely consistent with the previously measured R_h results. Meanwhile, the Sld (ρ) of TA@DAP also remarkably increased from 9.81 to 9.89 $10^{-6}/Å^2$, implying that TA has been successfully modified to the particles, in accordance with the results reported by other literature

Table 1
Structural parameters of DAP and TA@DAP nanoparticles obtained from model fits to the coherent SAXS curves.

Sample	R_{np} (nm)	PDI	Sld ($10^{-6}/Å^2$)	R_{HS} (nm)	η (%)	ξ (nm)
DAP	12.40 ± 0.11	0.28	9.81 ± 6.81 × 10^{-5}	21.90 ± 0.02	12.4 ± 0.0002	1.36 ± 0.02
TA@DAP	13.62 ± 0.07	0.23	9.89 ± 6.20 × 10^{-5}	22.16 ± 0.01	11.4 ± 0.0001	2.76 ± 0.01

[48]. In addition, the hard-sphere radius (R_{HS}) was upregulated from 21.90 ± 0.02 nm to 22.16 ± 0.01 nm, which means that TA@DAP has a more uniform particle size distribution, higher particle dispersity, and larger inter-particle distances, possibly caused by the modification of TA molecules with steric hindrances in the outer layer of the particles [49]. A small shift in the volume fraction (η) of associated particles, i.e., from 12.3 % to 11.4 %, also corroborated the relatively looser dispersion of the DAP nanoparticles after TA modification [50]. Furthermore, the Ornstein-Zernike equation in Equation (8) was employed to describe the scattering curves, demonstrating the mean chain-to-chain distance (correlation length, ξ) inside these nanoparticles increased from 1.36 ± 0.02 nm to 2.76 ± 0.01 nm. The upward ξ suggests that the TA@DAP spheres may cause inside local chain aggregation or larger chain spacing due to the diffusion of partial TA into the interior of the particle. Literature also reported that an increased ξ in polyurethane nanomaterials denoted enhanced distances between crystalline segments of the polymer chains [51] or greater crystalline thickness [52], as a potential direction for subsequent research. The Guinier equation (Equation (6)) was utilized to calculate the radius of gyration (R_g) and the shape factor (R_g/R_h ratio) of both particles, further confirming the morphological changes of the particles after TA modification. The R_g is 10.5 ± 0.08 nm for DAP and is 11.4 ± 0.12 nm for TA@DAP (Equation (7)). Meanwhile, the shape factors for DAP and TA@DAP are 0.88 and 0.80, respectively. The shape factor reports on molecular shape. For a hard sphere, the ideal R_g/R_h value is 0.77 [30]; whereas the closer the factor is to 0.77, the better the ideal spherical shape approaches [53]. All the above results on the characterization of TA-modified DAP nano-crosslinkers support the successful modification of DAP by TA. Particularly, the advanced scattering techniques and curve parameter fitting reveal the influence of TA on DAP nanostructures.

3.2. Preparation, optimization, and characterization of self-healing hydrogels

The possible variations produced by TA modification of DAP and the potential gelling mechanism of CTDP hydrogels crosslinked by dynamic Schiff base linkages are illustrated in Fig. 3A. The hydrogel was prepared by dynamic Schiff base, i.e., a reversible chemical linkage reacted through an amino group and an aldehyde group. The concentration of TA@DAP crosslinker used in the CTDP hydrogel is 2 wt%, which is based on our previous study regarding the optimal formulation of DAP crosslinker with CMC hydrogel [20]. In earlier findings, when the concentration of DAP was over 2 wt%, the hydrogel produced a large amount of inhomogeneous aggregates during the crosslinking process. The selection of CMC concentration is mostly limited by its water solubility, i.e., maximum 2 wt% in water, so the highest concentration of the main chain is chosen for achieving relatively higher modulus and slower degradation. In the present work, we have tried to gelate TA@DAP with CMC at a concentration higher than 2 wt%, but we encountered the same inhomogeneous aggregation as that of the unmodified DAP crosslinker. When the DAP concentration is larger than 2 wt%, intense local crosslinking can occur, and the crosslinking process is not in optimal equilibrium. Meanwhile, the CTDP hydrogel selected for further studies contained 2 wt% CMC and 2 wt% TA@DAP. From the macroscopic gel formation observation, CTDP hydrogel based on CMC and TA@DAP rapidly formed in ~7 min, which was shorter than that of DAP-crosslinked CDP hydrogels (~12 min), implying that extensive hydrogen bonding in the TA-modified TA@DAP might assist the crosslinking [20,54]. Since the TA in TA@DAP dispersion is mostly complexed into the particle system due to physical interactions, there may exist free TA in the system. However, because TA can also produce hydrogen bonding with CMC, any possible free TA can be integrated into the gel system instead of remaining the free state [55,56]. Macroscopically, CTDP hydrogel performed good injectability, self-healing, and self-adaptability, as shown in Fig. 3B. CTDP hydrogel can be extruded through 30-gauge needle (0.15 mm inner diameter) into a star-shaped mold and subsequently formed an integrated hydrogel with smooth appearance. Upon chopping the hydrogel into separate small pieces, the fractured hydrogel pieces self-healed and further recovered its original shape into an integrated clipable hydrogel within ~35 min. These macroscopic experiments demonstrated the good shape adaptability and self-healing properties of the resulted hydrogel. The SEM images of the hydrogels are shown in Fig. 3C and D. The cross-sectional pore structure of CTDP hydrogels was more uniform compared to CDP hydrogels, which may be related to the strong hydrogen bonding of TA to assist crosslinking. In addition, CDP hydrogel degraded faster than CTDP hydrogel within 14 days (Fig. 3E), which also is probably associated with the hydrogen bonding-mediated crosslinking.

The mechanical properties of soft hydrogels were mostly investigated through rheological measurements (Fig. 3F). The physical sol-to-gel transition ($G' \geq G''$) existed at ~380 s for CTDP hydrogel, which is nearly consistent with the macroscopic gelling time. The modulus of the CTDP hydrogel was stable in the time sweep, with a G' value of about 180 Pa. This indicates that the hydrogel primarily has an elastic-dominated three-dimensional network structure. When the dynamic strain varied from 200 to 800 %, the strain-induced gel-to-sol transition occurred at the strain of ~660 % for the CTDP hydrogel, demonstrated as Fig. S4. The damage-healing cycles were conducted at alternating strains of 1 % and 700 % for CTDP hydrogel. After several repeated cycles, the hydrogel recovered approximately 100 % its original modulus after structural damage induced by high strain within 3 min, indicating good and rapid self-healing ability. Furthermore, the steady-shear tests of the hydrogel revealed that the viscosity of the hydrogels decreased with an increasing shear rate, exhibiting shear-thinning behavior for good injectability. The macro-injectivity is confirmed by fluent writing words in Fig. 3I. Moreover, the ROS scavenging assay (Fig. 3J and K) showed that TA@DAP nano-crosslinker and TA@DAP-crosslinked CTDP hydrogel exhibited lighter shades of purple compared to the negative-control group (only DPPH solution, named CN), DAP nanoparticle, or CDP hydrogel, with a decrease in the characteristic absorption of DPPH being observed at 517 nm. These results suggested that the modification of TA endowed the nano-crosslinker and the hydrogel with ROS-scavenging properties, which may be attributed to the rich phenol groups [21]. The above findings verify that the addition of TA positively contributes to the regulation of structural homogeneity and endows the resulted CTDP hydrogel with anti-oxidative capability, while maintaining the original smart properties of CDP hydrogel.

3.3. Cell culture and in vitro capabilities of antioxidation and anti-inflammation

Cell experiments were carried out using Transwell chambers in 24-well plates. Cell viability was analyzed via CCK-8 assay on the first three days of culture (Fig. 4A). All groups showed high cell viability, i.e., no less than 100 % versus the initial day, and the CTDP hydrogel showed the highest cell proliferation rate (~195 %) among all groups. The in vitro cellular inflammation was modeled by LPS stimulation of NE-4C NSCs, referring to our previous publication. First, cellular level antioxidant capacity was initially characterized by testing total SOD levels in treated NSCs utilizing the SOD assay kit, as shown in Fig. 4B. The CTDP hydrogel and TA@DAP-treated groups exhibited a significant recovery of SOD activity (42.20 U/mg protein and 46.59 U/mg protein), without clear difference between them. The production of intracellular ROS was then stained with DCFH-DA using the commercial ROS assay kit (Fig. 4C) and quantified by the fluorescence intensity in Fig. S5. The CTDP hydrogel and TA@DAP-treated groups performed remarkably lower fluorescence intensities than the LPS-treated group (over 90 % reduction), but without statistical significance. Although the addition of TA improved the capacity of hydrogels to scavenge ROS optimally, over 2-fold in fluorescence intensity with healthy NE-4C NSCs was still observed. The clearance ability of ROS from TA is mainly driven by its

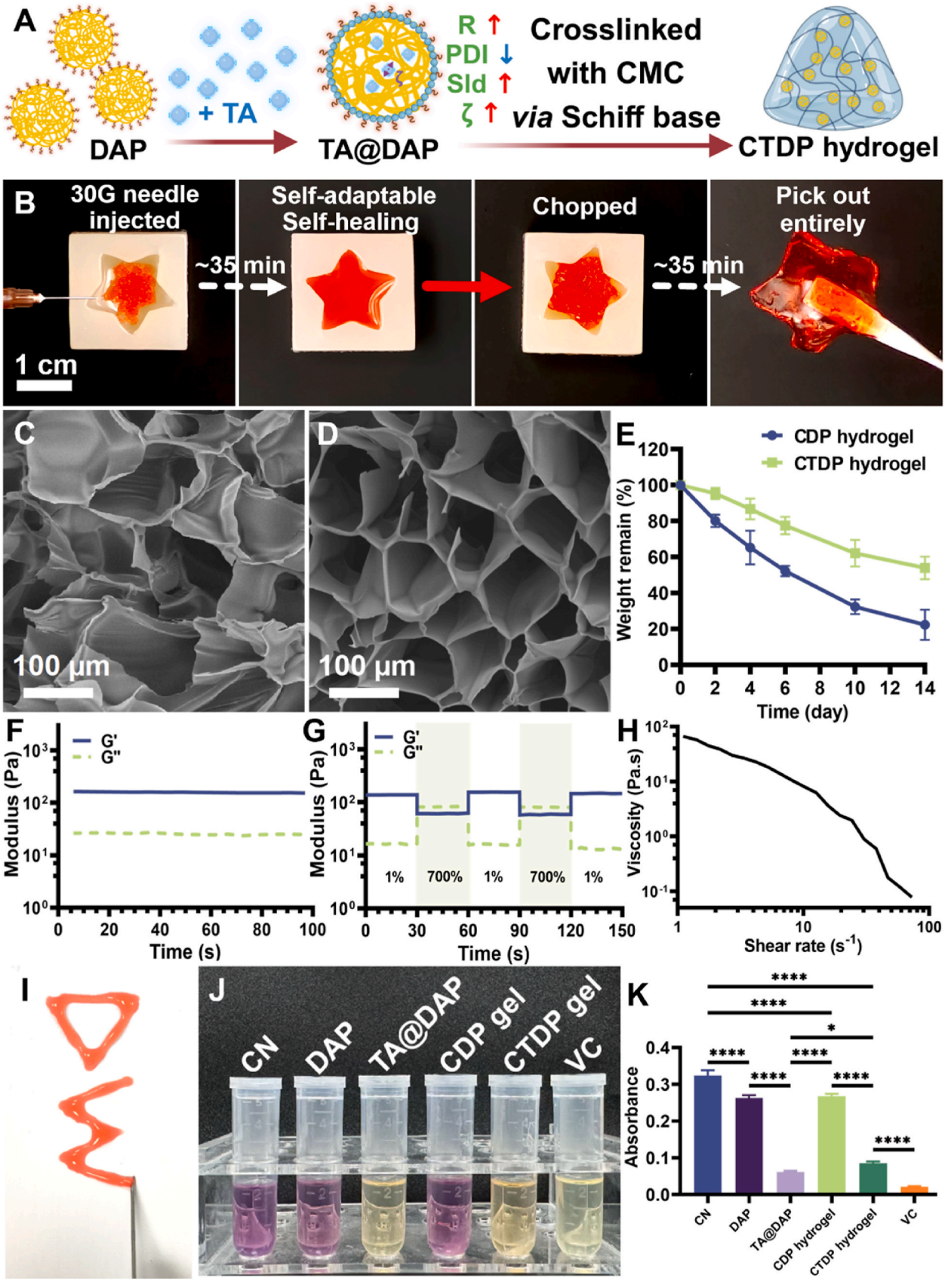

(caption on next page)

Fig. 3. Synthetic chemistry, preparation, morphology, and characterization of the CTDP hydrogel. (A) Schematic diagram for the possible TA modification changes on DAP into TA@DAP and the potential gelation mechanism of the CTDP hydrogel. Images created with BioRender.com. (B) The CTDP hydrogels can be injected through 30-gauge syringe needles with 150 mm internal diameter into the star-shaped mold. An integrated star-shaped hydrogel with smooth and homogenous appearance formed after self-adaption and self-healing for ~35 min at 25 °C. The integrated hydrogel was chopped into small pieces and then refilled the star-shaped mold. The star-shaped hydrogel self-healed for 35 min and recovered into its original shape. The SEM image for the cross-section of (C) the CDP hydrogel and (D) the CTDP hydrogel. (E) Remaining weights of the CDP and CTDP hydrogel in PBS at 37 °C. (F) Time-sweep experiments showing the storage moduli (G′) and loss moduli (G″) of the hydrogel against the gelling time at 1 Hz frequency and 1 % dynamic strain. (G) Self-healing experiments showing the G′ and G″ values of the equilibrium hydrogels at 1 Hz frequency and alternate continuous damage-healing cycles of 1 % and 700 % dynamic strains at 25 °C. (H) The steady shear-thinning properties of the hydrogel determined by measuring the viscosity versus shear rate. (I) The hydrogels can be injected through 30-gauge syringe needles to write letters. (J) Photos for color changes of DPPH solution (CN, negative control) after free radical scavenging by various groups, including DAP, TA@DAP, CDP hydrogel, CTDP hydrogel, and Vitamin C (VC, positive control). (K) The absorbance of DPPH solutions in each group were detected via UV–vis. Data are represented as mean ± SD (n ≥ 3). *$p < 0.05$ and ****$p < 0.0001$ between the indicated groups. (For interpretation of the references to color in this figure legend, the reader is referred to the Web version of this article.)

rich phenolic hydroxyl groups [57], and can regulate multiple antioxidant-related cellular pathways, such as ROS-ERK/NF-κB pathway and the recovery of mitochondrial damages [58–60]. Meanwhile, the in vitro anti-inflammatory ability of CTDP hydrogels was verified by IF staining (Fig. 4D) and WB (Fig. 4E) using LPS-stimulated BV2 cells, including IL-1β for M1 phenotype and CD206 for M2 phenotype. The average fluorescence intensity of IF was quantified in Fig. S6, while the WB bands were visualized in Fig. 4F and G. Results from the IF experiments showed that the CTDP hydrogel and TA@DAP nanoparticle-treated groups exhibited the lowest IL-1β intensities as well as the highest CD206 intensities among the other groups, except for the control group (healthy cells), while the CTDP hydrogel was significantly more effective than the TA@DAP nanoparticles with a potentially better anti-inflammatory effect. Further, the experimental results of WB were consistent with the results demonstrated by IF. Moreover, other inflammatory factors of the M1 phenotype, including TNF-α and iNOS, were also validated by WB experiments, all of which were compatible with the trend of IL-1β results. The WB bands are shown in Fig. 4H as well as the corresponding quantification presented in Fig. 4I and J. All the uncropped images for WB in Fig. 4 are presented in Fig. S7. CTDP hydrogels exhibited the optimal anti-inflammatory effect and had the potential to turn M1-phenotype towards M2-phenotype induction. DAP has been confirmed in our previous studies to be an effective anti-inflammatory and to promote the conversion of M1-phenotype macrophages to M2-phenotype at their zeta potentials above −40 mV [19,20]. The enhanced electrostatic surface zeta potential can contribute to the anti-inflammatory effect of nanoparticles at the macrophage level, also clearly reported in other literature [61,62]. After additional modification of DAP with the natural strong antioxidant molecule TA, the zeta potential of TA@DAP was maintained at about −42 mV, which was also experimentally determined not to affect but to enhance the anti-inflammatory function of DAP itself. Moreover, TA has also been investigated to promote macrophage polarization from M1 phenotype to M2 phenotype [63], which partly supports a clear increase in the anti-inflammatory effect of TA@DAP and CTDP hydrogels compared to the groups without TA modification.

3.4. Efficacy evaluation by the PD rat model

The therapeutic efficacy of CTDP hydrogels was systematically investigated in a unilateral 6-OHDA-induced PD rat model (Fig. 5A). Compared to the classical N-methyl-4-phenyl-1,2,3,6-tetrahydropyridine (MPTP)-induced mouse model, the 6-OHDA-lesioned rat model offers superior stability in replicating dopaminergic neurodegeneration and persistent motor deficits, with pathological progression closely mirroring human PD pathophysiology [27]. Despite its translational relevance, the application of 6-OHDA-induced PD models in assessing biomaterial-based therapeutic interventions remains limited due to the technical demands of stereotaxic surgery and the requirement for secondary intracranial administration [64]. The 6-OHDA-induced PD model is representative in simulating DAcNs deficits and reflects the movement disorder symptoms of PD, but factors such as abnormal aggregation of α-synuclein (α-syn) and mitochondrial dysfunction are difficult to simulate. The CTDP hydrogel system used in this study to treat PD targeted progressive pathological changes and mainly served to protect neurons and alleviate neuroinflammatory modulation of behavioral abnormalities. Subsequently developed biomaterials are also expected to be multidimensionally designed to target different pathogenic mechanisms.

In the present study, the recovery of motor function in PD rats treated with a medicated hydrogel was assessed using two behavioral tests, i.e., the cylinder test (Fig. 5B) and the circling speed test (Fig. 5C). After 14 days of treatment, all groups experienced a significant decrease in the number of turns per minute of counterclockwise rotation, except for the saline group. The relief was most pronounced in the TA@DAP nanoparticle as well as CTDP hydrogel-treated group among all groups and was accompanied by exploration of the ipsilateral side. A statistical difference was also observed between the two groups at 14 days (6.67 turns/min for TA@DAP vs. 5.67 turns/min for CTDP hydrogel, respectively). Healthy rats in the sham operation group did not show the same side rotational behavior after the APO injection, so the rate of circling in the sham group was not included in the comparison. Compared to the saline-treated group (<3 %), all treatment groups achieved a marked improvement in the contact ratio of the forelimb on the damaged side, i.e., >10 %. Forelimb utilization of rats in the CTDP hydrogel and TA@DAP treatment groups recovered to ~32 % and ~23 %, respectively, with the addition of TA providing a distinct therapeutic effect rather than that of the DAP and CDP hydrogel treatment groups. Although the forelimb contact rate in the CTDP hydrogel group was lower than that in the sham group (~50 %), the behavioral abnormalities were alleviated. The lower percentage of rats using the injured forelimb in the saline group suggests that motor function was not obviously recovered. The functional improvement may be related to the strong ROS/Fe ions-scavenging properties of TA, which works as neuroprotection for neurodegenerative diseases [23,59].

The excessive neuronal bursts of STN discharge in the brain is a patho-electrophysiologic finding in PD and is causally related to Parkinsonian dyskinesia [65]. Neuronal discharges in the STN region were recorded in each group after 14 days and displayed in Fig. 5D, and spike rates within 30 s were counted and exhibited in Fig. 5E. The STN discharge spike rate was remarkably higher in the experimental group (>15 counts/s) than in the sham group (~15 counts/s) after a 14-day treatment. The saline-treated rats showed an approximately 6-fold increase in spike rate. In contrast, the TA@DAP nanoparticle and CTDP hydrogel-treated groups showed relatively low spike rate elevations (~40 counts/s and ~30 counts/s), indicating that the STN irregular discharges were effectively alleviated and prevented the further development of PD. Since the motor cortex is the target of SNc dopaminergic innervation [66], the biomaterials used as implants in this study may alleviate PD symptoms mainly due to the bioactivity of TA thereby achieving neuroprotection as well as affecting the nerve cell rhythms of the STN in the SNc projection area. Very recently, PD treatment by a conductive hydrogel based on polydopamine-modified polyurethane has also been reported [34]. The impaired forelimb contact rate in the

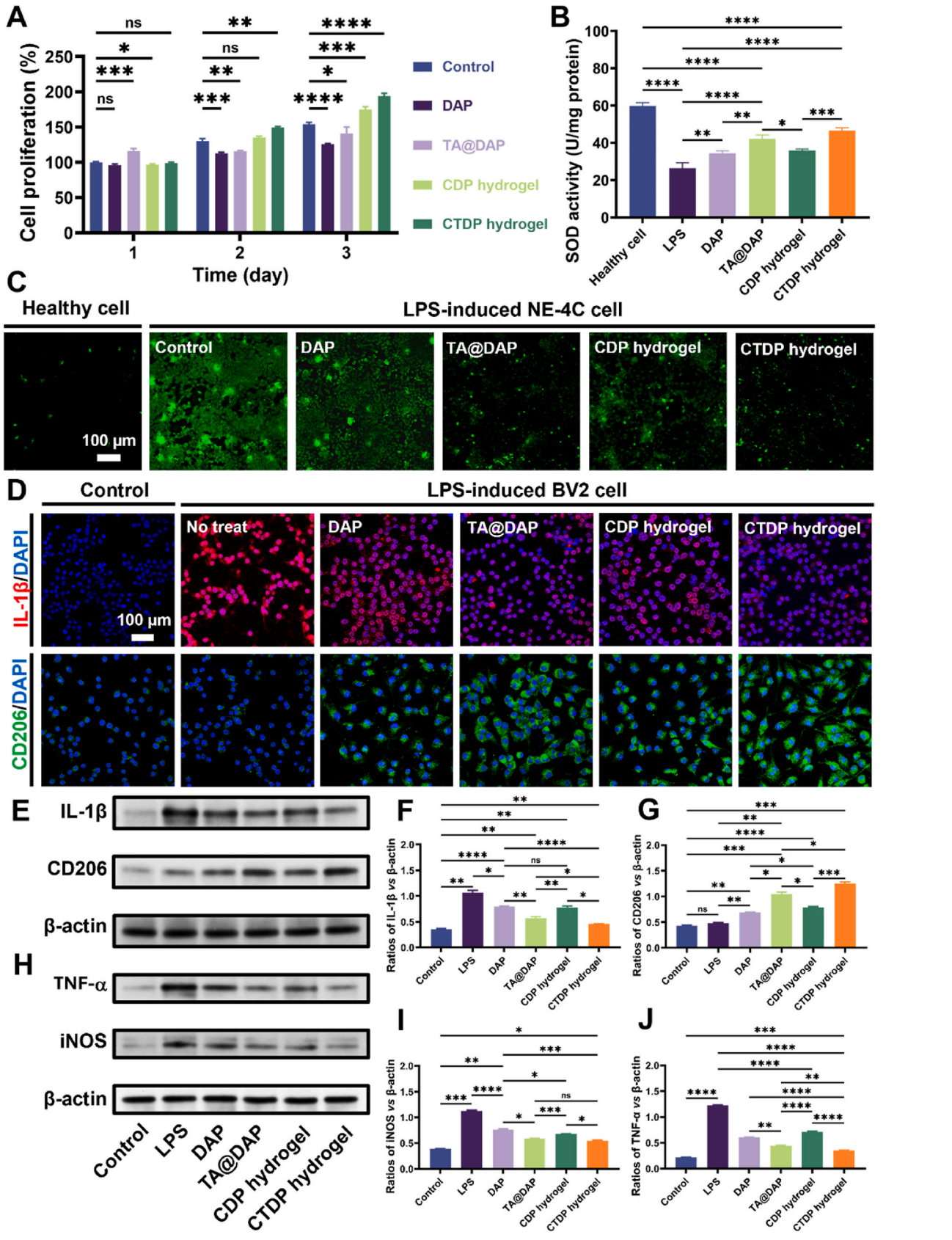

(caption on next page)

Fig. 4. In vitro cellular experiments of proliferation, antioxidation, and anti-inflammation. (A) Cell proliferation of NE-4C NSCs co-incubated using Transwell chambers with DAP, TA@DAP, CDP hydrogel, and CTDP hydrogel measured by CCK-8 assay during a culture period of 3 days. The proliferation was normalized to the value at day 0 and expressed as the percentage of the cell proliferation (%). As for antioxidative capability, NE-4C NSCs were stimulated by LPS to produce rich ROS. (B) Quantification of total SOD activity assay of LPS-induced NE-4C NSCs after co-incubation with each group for 24 h. (C) ROS visualization of microscopic fluorescent images in LPS-induced NE-4C NSCs and each group treatment by DCFH-DA staining. As for anti-inflammatory capability, BV2 microglia were pre-induced by LPS towards inflamed M1 phenotype. (D) Immunofluorescent images of LPS-induced BV2 microglia stained for IL-1β and CD206 after a 12-h treatment. (E) Western blot (WB) analysis for IL-1β and CD206 were validated. Densitometric analysis for the protein expression of (F) IL-1β, and (G) CD206 normalized to that of β-actin. (H) WB analysis for extra inflammatory factors, i.e., TNF-α and iNOS, were performed. Densitometric analysis for the protein expression of (I) iNOS and (J) TNF-α normalized to that of β-actin. Data are represented as mean ± SD (n ≥ 3). $^{*}p < 0.05$, $^{**}p < 0.01$, $^{***}p < 0.001$, and $^{****}p < 0.0001$ between the indicated groups.

conductive hydrogel-treated group was about 35 %, which was similar to the treatment results of the CTDP hydrogel-treated group in the current study (~32 %). Electrophysiological results of the neuronal discharge spike rate in the STN region in the conductive hydrogel-treated rat brain was about 28 counts/s, also quite similar to the CTDP hydrogel treatment results. The therapeutic mechanisms of CTDP hydrogel, however, may be different from that of the reported hydrogel, i.e., CTDP hydrogel being linked to the bioactivity of TA and the reported hydrogel being associated with its microconductivity [67]. A ceiling effect thus may exist when treating PD by in situ administration of a tiny amount of hydrogel (4 μL). A future direction to prepare hydrogel is to combine bioactive molecules and microconductive properties in order to overcome the bottleneck of therapeutic efficacy. As for the prospective translational medicine, the administration needs to be significantly increased, so there are still multiple challenges to be conquered in the future.

The tissue sections of brain were first analyzed via H&E staining (Fig. S8). After 7 days of injection, nearly complete degradation of the hydrogel was observed in the coronal tissue sections, with some traces and a small number of immune cells. Later at 14 days after the injection, the immune cells in the coronal tissue sections were restored to normal levels. The in vivo degradation rate was slightly faster than the in vitro degradation results, which may be related to the inflammatory environment. The ex vivo fluorescent imaging of FITC-labeled CTDP hydrogels in the brain after in situ injection at 3, 7, and 14 days are presented in Fig. S9. The intensity of diffusion via the fluorescent marker revealed that the intensity was the highest on day 3 and effectively diffused to nearly the entire brain, with some intensity remaining by day 14 but relatively weak. The fluorescent marker diffusion may be related to degradation of the hydrogel. Histological staining showed significant changes in TH, one of the rate-limiting enzymes in dopamine biosynthesis and a featured indicator of PD in brain tissue sections. After a 14-day in situ implantation of the hydrogel, differences in the expression levels of TH in the SNc and striatum in the brain were detected. Fluorescence images of TH-positive (TH+) DAcNs and DAcFs in SNc and striatum are shown in Fig. 6A and C, respectively, and semiquantitative data are summarized in Fig. 6B and D. The number of TH + DAcNs and fluorescence intensity were dramatically enhanced in the SNc of biomaterial-treated PD rats compared with the saline group, especially in the TA@DAP group and the CTDP hydrogel group. The fluorescence density of TH + DAcFs in the striatum showed the same trend. Also, the TA@DAP treated group and CTDP hydrogel-treated group revealed a statistically significant difference in TH + expression at 14 days. Furthermore, WB was performed to visualize and evaluate the protein expression of α-syn, as a PD characteristic pathological protein, in the SNc regions of rats (Fig. S10A and S10B). The uncropped images are presented in Fig. S10C. According to statistical analysis, the results of WB were mostly consistent with those of IF, where the TA@DAP and CTDP hydrogel-treated groups showed apparent alleviation of α-syn aggregation. Nonetheless, the CTDP hydrogel system is mainly designed for targeting neuroinflammation, and therefore the mechanism of mitigating α-syn aggregation is noteworthy but not discussed in depth.

Immunostaining was also performed for Iba1, a marker for microglia, and GFAP for astrocytes (Fig. 6E). The semiquantitative data in Fig. 6F and G demonstrated that the numbers of activated (Iba1+) microglia and GFAP + astrocytes were considerably higher in the saline-treated group than in the other groups as the course of PD progressed, and the numbers of Iba1+ microglia and GFAP + astrocytes were substantially reduced in the TA@DAP and CTDP-treated groups, suggesting that the two groups obviously reduce the neuroinflammatory response in the SNc region. In contrast, while the CTDP hydrogel-treated group showed elevated levels of Iba1+ microglia compared with the sham group, there was no significant difference in the levels of GFAP + astrocytes. The level of neuroinflammation in the brain of the PD rats was also verified by the level of tissue NO in Fig. 6H. The level of NO represented the development of neuroinflammation in the brain and the experimental results were in agreement with the trend obtained in IF staining. According to the literature, excess GFAP + astrocytes can exacerbate PD by generating an acidic inflammatory environment that promotes microglia formation and allows neuroinflammation to continue to develop, whereas moderate amounts of astrocytes release neuroprotective growth factors [35]. Further, one of the major contributors of 6-OHDA to PD is inducing massive production of ROS, which disrupts the function of neuronal mitochondria [68]. The antioxidant capacity of CTDP hydrogel in the brain was confirmed by the restoration of SOD activity (Fig. 6I). The results indicated that the SOD activity in the brain of the CTDP hydrogel-treated group was the highest (~50 U/mg tissue) among all treated groups, but still lower than that of the sham group by ~17 %. The above results confirmed the significant therapeutic effect of TA for the modification of DAP and subsequent preparation of bioactive hydrogel. TA as a natural antioxidant with phenolic groups was evidenced to possess the potential to target the NF-κB pathway for mediating neuroinflammation in PD [24,69], but few direct studies have been conducted on TA to confirm the therapeutic mechanism on PD. Taken together, these in vivo findings support that the administration of TA-modified DAP crosslinked bioactive CTDP hydrogel significantly alleviates 6-OHDA-induced PD, i.e., reduces the loss of DAcNs and DAcFs in the SNc and striatum, as well as decreases the neuroinflammatory response in the brain.

In situ injection of hydrogels to the mouse brain for the treatment of PD was first reported about 10 years ago, utilizing a biologically inactive hydrogel loaded with activin B [35]. Since then, some bioactive hydrogels have been developed but only varied in pairing with loaded drugs or stem cells, and only in vitro cellular tests have been done to give hypotheses for the treatment of PD [70]. Chitosan-based biodegradable self-healing hydrogels have been designed in recent years with various smart properties to assist in the treatment of PD and they have shown positive therapeutic effects in PD animals [20,27,33,34]. However, based on the current literature on the therapeutic effects of in situ injections, the upper limit of the therapeutic effect of hydrogel can be inferred, especially in the recovery of motor function and abnormal neuronal discharges, i.e., the speed of unilateral rotation >5 turns/s, the ratio of impaired forelimb contacts <35 %, and neuronal discharges of spike counts >30 counts/s. The therapeutic efficacy is likely to be limited by the amount of gel injected, as PD modeling does not have a substantial cavity in the brain to enhance the amount of gel injected, and the translation from small animals to the clinic is still hindered by a very large scale. The future prospect of hydrogel-assisted therapy still requires mounting of drugs or cells to achieve favorable therapeutic effects to bridge the cross-species scale barrier. Meanwhile, considering the

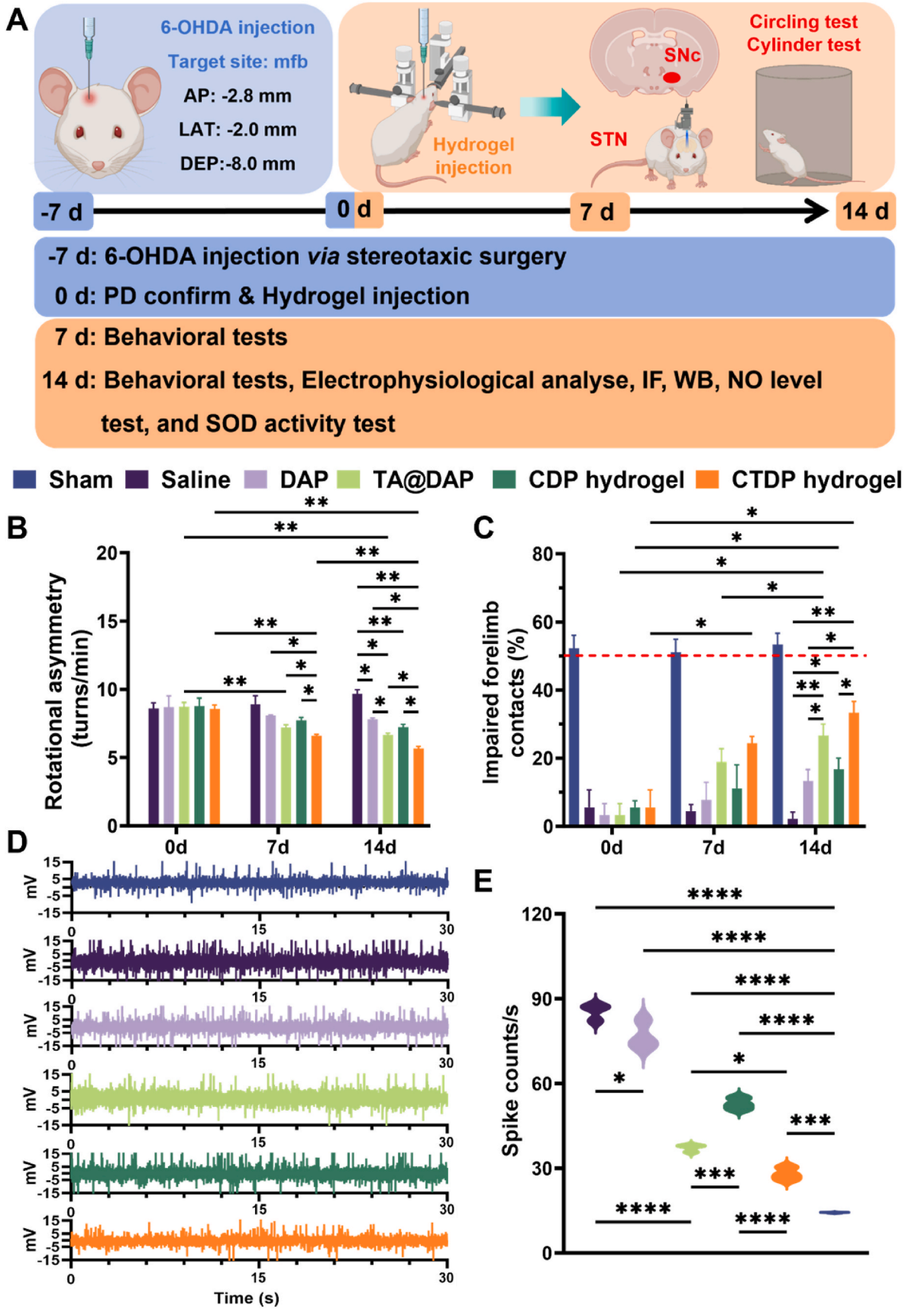

(caption on next page)

Fig. 5. Behavioral evaluation and electrophysiological analyses of PD rats treated by hydrogels. (A) Schematic illustration of the PD rat model. PD model was established by in situ injection of 6-OHDA into the mfb region of rat brains. After confirmation of PD induction, the nanoparticles or hydrogels were further injected into the lesion regions for 14 days, and the efficacy of treatment was evaluated through behavior tests, electrophysiological tests, immunofluorescent analyses, and WB analyses. Parts of images created with BioRender.com. (B, C) Quantitative assessment for the functional recovery of various treatment, including saline, DAP, TA@DAP, CDP hydrogel, and CTDP hydrogel, for PD rats as compared to the untreated PD rats (0 day, Sham group), based on (B) the rotational asymmetry speeds and (C) the impaired forelimb contact proportion. (D) Electrophysiological traces of STN spikes in each treating group within 30 s at 14 days. (E) Quantitative overall spike counts of each group from a 30-s period of each recording devoid of significant noise at 14 days. Data are represented as mean ± SD ($n \geq 3$). *$p < 0.05$, **$p < 0.01$, ***$p < 0.001$, and ****$p < 0.0001$ between the indicated groups.

limitations of in situ injection as a delivery method, bioactive injectable hydrogel could be a potential candidate for adjuvant therapy as an iteration of existing clinical tools, such as deep brain electrode implantation.

3.5. Network pharmacology and molecular docking

The network pharmacology approach was used to identify potential therapeutic targets of selected compounds by comparing them with disease-associated targets, yielding 18 overlapping targets (Fig. 7A). In Fig. 7B, we displayed the interactions between compounds, i.e., CMC, TA, and polyurethane, and potential targets by compound-target network. Furthermore, the PPI network demonstrated strong interactions among these targets, as shown in Fig. 7C. To explore the functional enrichment of compound targets, we performed the KEGG and Gene Ontology (GO) enrichment analysis. KEGG pathway enrichment analysis resulted in the enrichment of targeted genes in different signaling pathways, with significant enrichment in the NF-κB signaling pathway (Fig. 7D). Moreover, GO enrichment analysis revealed that the identified targets were significantly associated with various biological processes (BP), particularly immune-related functions such as leukocyte adhesion and chemotaxis (Fig. 7E). Cellular component (CC) enrichment analysis indicated that these targets were predominantly localized in membrane compartments, secretory granules, and microdomains (Fig. 7F). Furthermore, molecular function (MF) enrichment analysis demonstrated in Fig. S11A that the targets were mainly involved in carbohydrate binding, glycosaminoglycan interactions, and chemotaxis-related activities, suggesting their potential roles in immune modulation and extracellular matrix interactions. These findings provide theoretical insights into the potential mechanisms of action of the compounds investigated in disease treatment.

The Venn diagram highlights RIPK as a crucial link between the targeted genes and the NF-κB signaling pathway, further emphasizing its potential regulatory role in inflammation and immune signaling (Fig. S11B). Therefore, we performed molecular docking analysis in Fig. 8A and B, which revealed that both CMC and TA interact with RIPK1, and TA exhibits a stronger binding affinity (−9.7601 kcal/mol) compared to that of CMC (−6.4598 kcal/mol). The interaction analysis suggests that TA forms more stable interactions within the RIPK1 binding pocket, potentially leading to enhanced inhibitory effects. These findings indicate that TA may serve as a more potent modulator of RIPK1 activity, providing insights into its therapeutic potential in targeting RIPK1-related signaling pathways.

3.6. Targeting RIPK1 via NF-κB–IκBα pathway for PD treatment

We identified a promising pathway, the RIPK1-NF-κB-IκBα axis, based on network pharmacology as well as molecular docking results, which was validated by WB using SNc tissues from PD rats. The expression levels of RIPK1 and NF-κB p65 in the SNc region were firstly tested, and the bands are displayed in Fig. 8C, with the corresponding statistics summarized in Fig. 8D–F. The TA@DAP in this work operated as one of the main components of the hydrogel when the hydrogel met external cells or tissues. Simultaneously, the nanoparticles were released by fragmentation with the degradation of the hydrogel. The addition of TA treatment groups, including TA@DAP and CTDP hydrogel treatment groups, showed very significant suppression of RIPK1 in the tissue levels of rats, with CTDP hydrogel treatment being the best, but still having an upregulation of about 20 % from the sham group. The treatment groups with the addition of TA were also very marked for the activation of NF-κB p65, with the CTDP hydrogel group showing an approximately two-fold elevation compared to the saline group. As for the phosphorylated NF-κB p65 (p–NF–κB p65) index, the trend of inhibition was consistent with RIPK1. Meanwhile, IκBα as an important indicator for controlling NF-κB activity was also assayed [71,72], and the WB bands with their statistical results are shown in Fig. 8G–I. The uncropped bands of all WBs in the mechanism discussion are shown in Figs. S12 and S13. A rise in IκBα expression was clearly seen in the treatment group with the addition of TA, while the proportion of *p*-IκBα was downregulated, without statistical difference in expression within the two TA-included groups. The trend of IκBα is known to undergo a process of change in recovery from stimulation in the brain after a 14-day treatment and confirms the apparent anti-neuroinflammatory therapeutic effect of TA@DAP and CTDP hydrogels [73]. Combined with the modulation of inflammatory factors TNF-α and iNOS in the cellular level, we offer a possible mechanism for the treatment of PD by minimally invasive injection of CTDP hydrogel as shown in Fig. 8J.

Investigating whether the therapeutic effect of CTDP hydrogel is limited to the RIPK1-NF-κB-IκBα pathway is also worthwhile. Previous studies have shown that TA has the ability to modulate apoptotic behavior [74]. WB tests for classical apoptotic markers were performed on brain tissues in the SNc region, including Cleaved-Caspases 3, Bax, and Bcl-2. Summarized WB bands and their uncropped bands are displayed in Fig. S14. Both the treatment groups with the addition of TA, i.e., the TA@DAP and the CTDP hydrogel groups, showed significant attenuation of apoptotic behavior, which is consistent with the results in the previous literature and probably suggests the possibility of other potential pathway modulation, such as ferroptosis-related pathway. Meanwhile, the hypothesis of anti-apoptosis and anti-inflammation as synergistic therapeutic benefits has been reported including that down-regulation of Caspase 3 is effective in avoiding DAcNs apoptosis [75], and that low levels of Cleaved-Caspase 3 can also protect neurons [76]. However, the above does not detract from the main idea of exploring the mechanistic pathways of biomaterials to treat diseases based on network pharmacology as a guide, as proposed in this work. Few existing studies of in situ injection of bioactive hydrogel alone for PD treatment have given clear mechanistic pathways, and the present study offers a possible direction to identify potential therapeutic mechanisms through the tools of network pharmacology combined with molecular modeling in conjunction with in vitro and ex vivo experiments.

The findings of this study collectively suggest that the newly designed TA@DAP nano-crosslinkers for preparing bioactive CTDP hydrogel exert therapeutic effects on PD. First, a simple bioactive molecules modification strategy was utilized and advanced coherent SAXS with data modeling was employed to characterize the nanoscale inner and intra structure changes of nanoparticles, which may provide considerable reference for other similar nanoparticle characterizations. As for the cellular level, the amounts of inflammatory factors in LPS-stimulated macrophages decreased significantly after hydrogel treatment. Promising therapeutic effects were observed with tiny hydrogel injection of 4 μL. Also, CTDP hydrogel, as a composite gel, has identified possible mechanistic pathways through network pharmacology and molecular docking, which provides a good example for hydrogel to

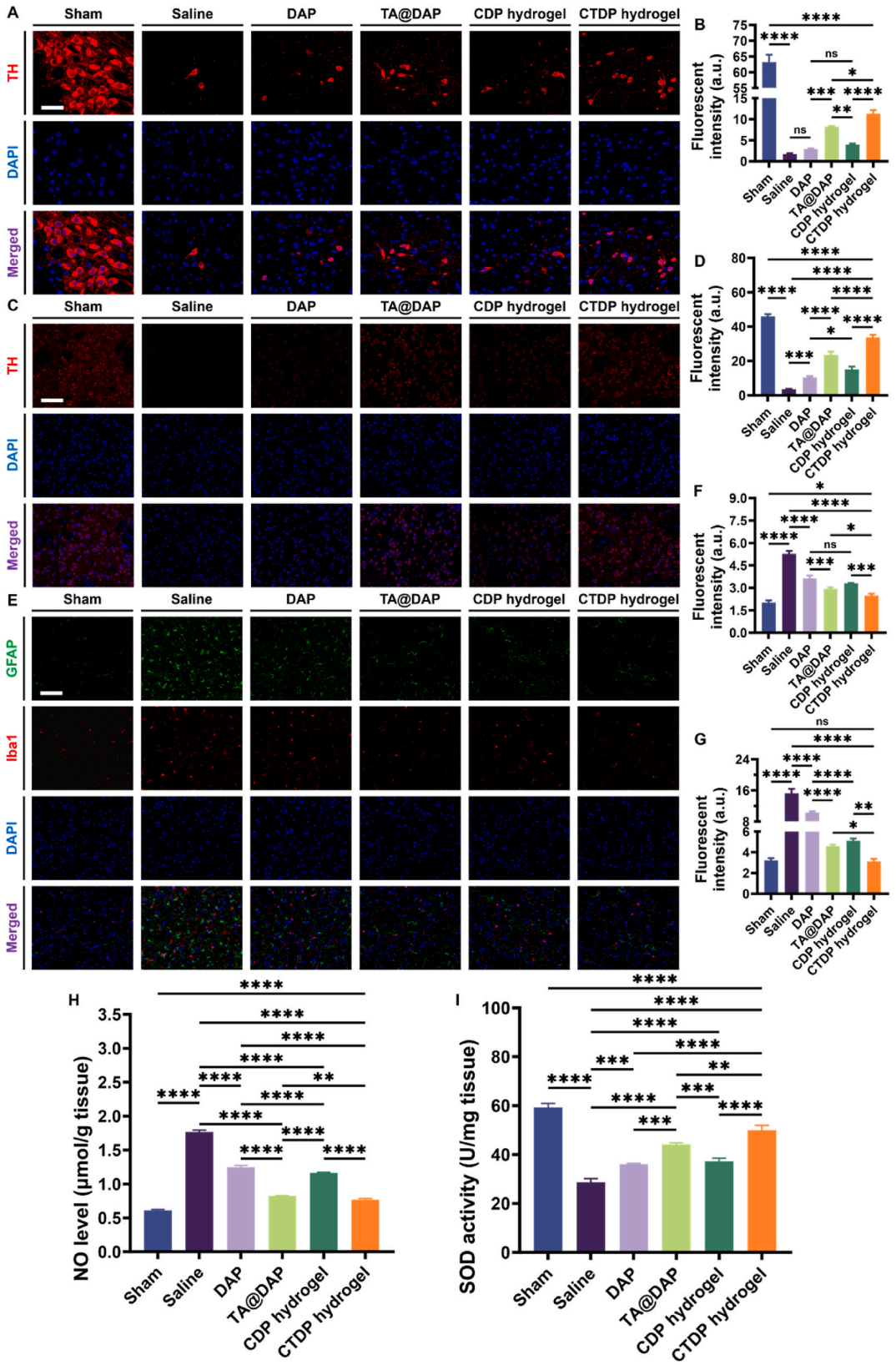

Fig. 6. In vivo histological analyses for PD specific marker and neuroinflammation in SNc and striatum. The expressions of TH + DAcNs in SNc (A) and TH + DAcFs in striatum (C) were investigated after the second surgery injection for 14 days. The average fluorescent intensities were quantified and presented as graphics for TH + DAcNs in SNc (B) and TH + DAcFs in striatum (D) of each group. (E) Fluorescent images of Iba1+ microglia (red) and GFAP + astrocytes (green) after implantation in the brain for 14 days. Quantification for the fluorescent intensity of (F) Iba1+ microglia and (G) GFAP + astrocytes in vivo. Both scale bars represent for 40 μm. (H) NO production levels in SNc region of rat brain after treatment were detected. (I) Quantification of total SOD activity in SNc region of rat brain after treatment was investigated for in vivo antioxidative capability. Data are represented as mean ± SD (n ≥ 3). *$p < 0.05$, **$p < 0.01$, ***$p < 0.001$, and ****$p < 0.0001$ between the indicated groups. (For interpretation of the references to color in this figure legend, the reader is referred to the Web version of this article.)

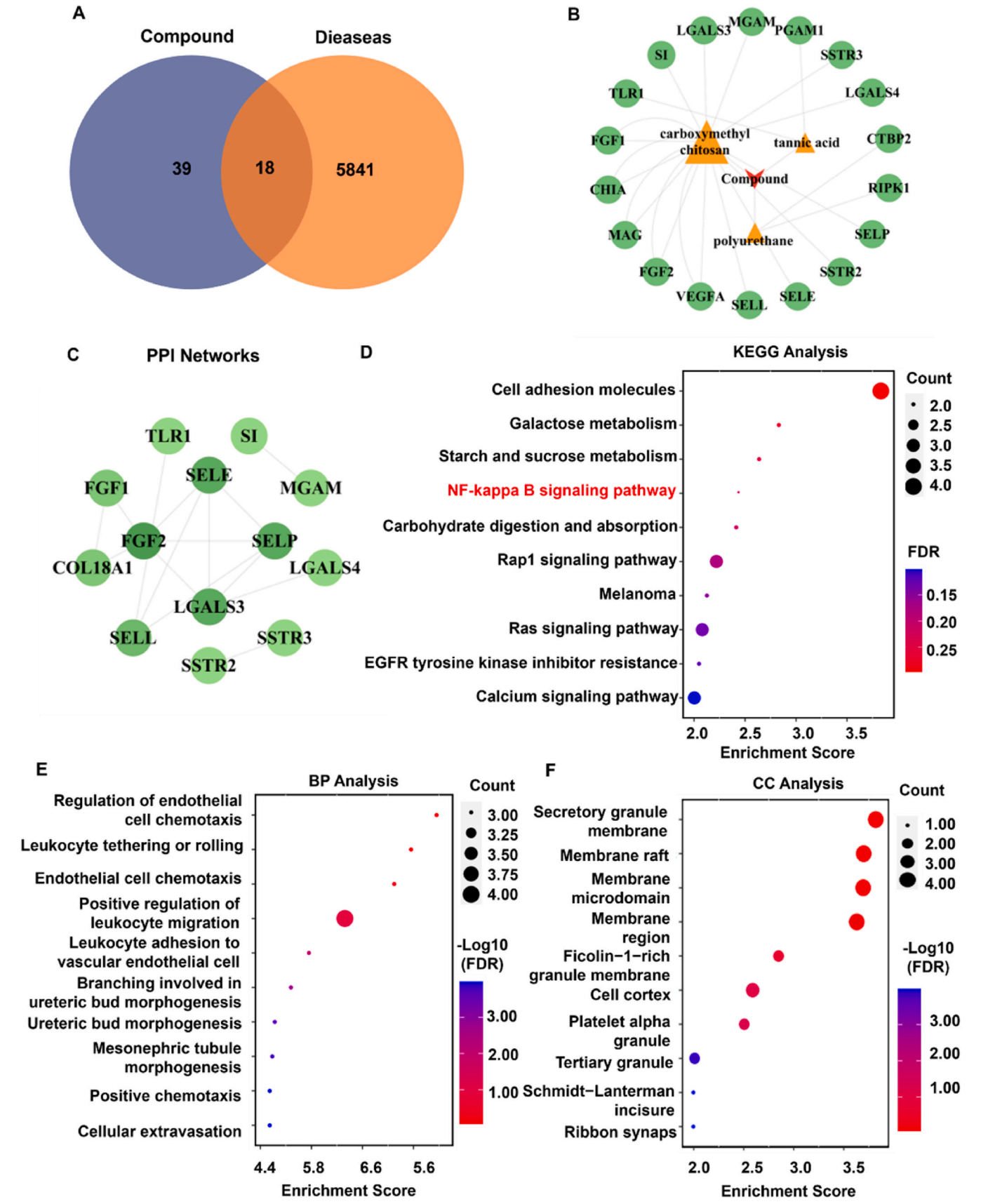

Fig. 7. Network pharmacology-based analysis of compound-disease targets and enrichment pathways. (A) Venn diagram showing the intersection of compound-related targets and disease-related targets. (B) Compound-Target Network displaying the interactions between compounds (carboxymethyl chitosan, tannic acid, polyurethane) and potential targets. (C) Protein-Protein Interaction (PPI) network. (D) KEGG pathway enrichment analysis. (E) Biological Process (BP) and (F) Cellular Component (CC) enrichment analysis.

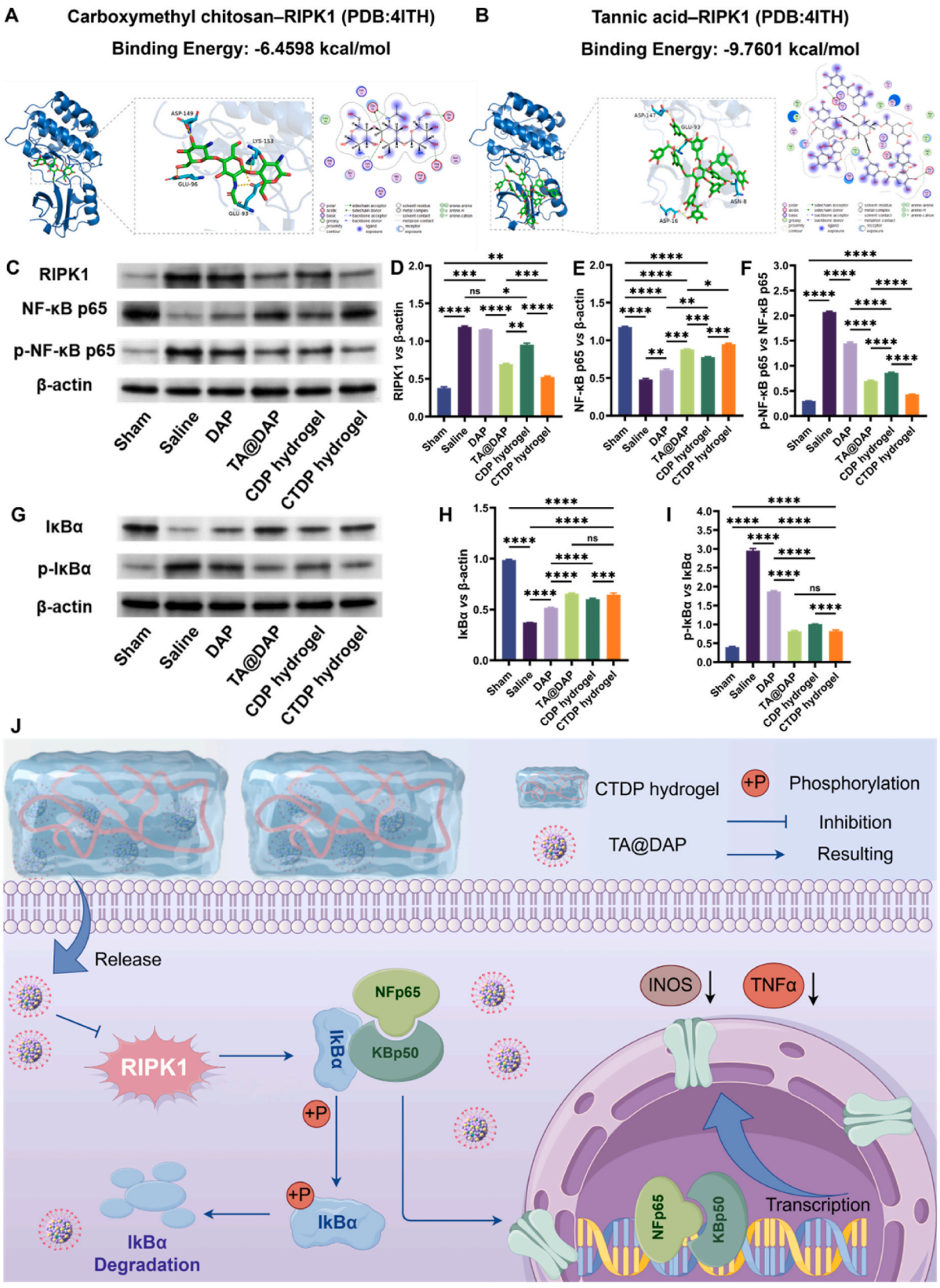

Fig. 8. Molecular docking for RIPK1 and validation of potential regulation pathway. Molecular docking results of (A) CMC and (B) TA with RIPK1 and binding energy. Potential RIPK1-NF-κB-IκBα pathways were identified and relevant indicators were confirmed by WB. (C) WB analysis of tissue proteins extracted from post-treated rat brain for RIPK1, NF-κB p65, and p–NF–κB p65 were tested. Densitometric analysis for the protein expression of (D) RIPK1 vs β-actin, (E) NF-κB p65 vs β-actin, and (F) p–NF–κB p65 vs NF-κB p65. (G) WB analysis of tissue proteins extracted from post-treated rat brain for IκBα and *p*-IκBα were further conformed. Densitometric analysis for the protein expression of (H) IκBα vs β-actin and (I) *p*-IκBα vs IκBα. Data are represented as mean ± SD (n ≥ 3). $^{*}p < 0.05$, $^{**}p < 0.01$, $^{***}p < 0.001$, and $^{****}p < 0.0001$ between the indicated groups. (J) Schematic representation of the potential mechanism of CTDP hydrogel for treating PD. Images created with Figdraw.com.

explore therapeutic mechanisms rather than simply discussing therapeutic effects. Although not all therapeutic mechanisms may be obtained through this approach, it can lower the threshold for materials science researchers to cross the field and make it easier to identify worthwhile targets in cross-disciplinary research. Through this work, the CTDP hydrogel serves as a promising candidate for developing a new generation of therapeutic strategies targeting neurodegenerative diseases.

4. Conclusion

New TA-modified DAP particles as efficient nano-crosslinkers were synthesized and well characterized through coherent SAXS integrated with data modeling. TA@DAP nanoparticles showed relatively more homogeneous PDI (0.23 *vs* 0.28 of DAP) and more spherical shape factor (0.80 *vs* 0.77 of ideal particle). An injectable chitosan-based CTDP hydrogel crosslinked with TA@DAP were engineered to treat PD, possessing proper modulus (~180 Pa), tiny needle injectability (30-gauge), and rapid self-healing (~100 %) properties. In vitro experiments confirmed the ability of CTDP hydrogel to scavenge ROS, promote NSC viability, and reduce the inflammatory factors. In vivo, administration of CTDP hydrogel in PD rats alleviated motor deficits, preserved DAcNs in the SNc and striatum, alleviated the irregular discharge of nerve cells in the intracerebral projection area, and reduced neuroinflammation. Network pharmacology and molecular docking elucidated and validated the role of TA in targeting RIPK1, thereby inhibiting downstream inflammatory pathways, i.e., RIPK1-NF-κB-IκBα. These findings lay the foundation of strategies for developing multifunctional hydrogels targeting neurodegenerative diseases through precision medicine approaches and may also lead to new insights for exploring therapeutic mechanisms for composite biomaterials.

CRediT authorship contribution statement

Junpeng Xu: Writing – original draft, Visualization, Validation, Project administration, Methodology, Investigation, Funding acquisition, Conceptualization. **Chaohui Guo:** Writing – original draft, Visualization, Validation, Investigation, Formal analysis, Data curation. **Guangshuai Zhou:** Writing – original draft, Visualization, Validation, Investigation, Formal analysis, Data curation. **Haoman Chen:** Software, Resources, Formal analysis, Data curation. **Peng Dai:** Validation, Methodology, Investigation. **Chonghui Tang:** Resources, Methodology, Funding acquisition. **Shih-Ho Lin:** Methodology, Investigation, Data curation, Conceptualization. **Tsai-Yu Chen:** Methodology, Investigation, Data curation, Conceptualization. **Chen Zhang:** Investigation. **Fanxuan Chen:** Investigation. **Na Dong:** Investigation. **Caiyan Li:** Investigation. **Jie Pan:** Investigation. **Xianzhen Chen:** Resources, Methodology. **Ping Wu:** Writing – review & editing, Resources, Conceptualization. **Shengcun Li:** Writing – review & editing, Resources, Methodology. **Lihua Luo:** Validation, Resources. **Xiaokun Li:** Supervision, Resources. **Jianwei Shuai:** Supervision, Software, Resources. **Shan-hui Hsu:** Writing – review & editing, Supervision, Resources, Conceptualization. **Zhouguang Wang:** Supervision, Software, Funding acquisition.

Declaration of competing interest

The authors declare that they have no known competing financial interests or personal relationships that could have appeared to influence the work reported in this paper.

Acknowledgements

This work was supported by the Leading Innovative and Entrepreneur Team Introduction Program of Zhejiang (Grant Number: 2023R01002), National Natural Science Foundation of China (Grant Number: 82271629, 82301790, 12090052, U24A2014), Zhejiang Provincal Postdoctoral Science Foundation (Grant Number: ZJ2024168), Postdoctoral Fellowship Program of CPSF (Grant Number: GZC20241251), Ningbo Natural Science Foundation (Grant Number: 2024J359), and Zhejiang Provincial Department of Health Project (Grant Number: 2024KY389, CN2023006). We are also grateful to the National Synchrotron Radiation Research Center, Taiwan, R.O.C. (2023-1-137-2) and the TPS 25A1 beamline groups for providing the resources and technical support.

Appendix A. Supplementary data

Supplementary data to this article can be found online at https://doi.org/10.1016/j.biomaterials.2025.123614.

Data availability

Data will be made available on request.

References

[1] B.R. Bloem, M.S. Okun, C. Klein, Parkinson's disease, Lancet 397 (2021) 2284–2303, 10291.
[2] W. Poewe, K. Seppi, C.M. Tanner, G.M. Halliday, P. Brundin, J. Volkmann, A.-E. Schrag, A.E. Lang, Parkinson disease, Nat. Rev. Dis. Primers 3 (1) (2017) 17013.
[3] Y. He, J.-G. Wang, C.-Q. Gao, Validity of the diagnostic criteria for Parkinson's disease, Lancet 404 (2024) 652, 10453.
[4] E. Kip, L.C. Parr-Brownlie, Reducing neuroinflammation via therapeutic compounds and lifestyle to prevent or delay progression of Parkinson's disease, Ageing Res. Rev. 78 (2022) 101618.
[5] P. Chopade, N. Chopade, Z. Zhao, S. Mitragotri, R. Liao, V. Chandran Suja, Alzheimer's and Parkinson's disease therapies in the clinic, Bioengineering & Translational Medicine 8 (1) (2023) e10367.
[6] S.-Y. Lim, A.H. Tan, A. Ahmad-Annuar, N.U. Okubadejo, K. Lohmann, H.R. Morris, T.S. Toh, Y.W. Tay, L.M. Lange, S. Bandres-Ciga, I. Mata, J.N. Foo, E. Sammler, J.C. E. Ooi, A.J. Noyce, N. Bahr, W. Luo, R. Ojha, A.B. Singleton, C. Blauwendraat, C. Klein, Uncovering the genetic basis of Parkinson's disease globally: from discoveries to the clinic, Lancet Neurol. 23 (12) (2024) 1267–1280.
[7] K. McFarthing, G. Rafaloff, M. Baptista, L. Mursaleen, R. Fuest, R.K. Wyse, S.R. W. Stott, Parkinson's disease drug therapies in the clinical trial pipeline: 2022 update, J. Parkinsons Dis. 12 (2022) 1073–1082.
[8] N. Moriarty, C.L. Parish, E. Dowd, Primary tissue for cellular brain repair in Parkinson's disease: promise, problems and the potential of biomaterials, Eur. J. Neurosci. 49 (4) (2019) 472–486.
[9] J. Xu, S.-h. Hsu, Self-healing hydrogel as an injectable implant: translation in brain diseases, J. Biomed. Sci. 30 (1) (2023) 43.
[10] Q. Min, R. Tan, Y. Zhang, C. Wang, Y. Wan, J. Li, Multi-crosslinked strong and elastic Bioglass/chitosan-cysteine hydrogels with controlled Quercetin delivery for bone tissue engineering, Pharmaceutics 14 (10) (2022) 2048.
[11] Q. Ma, Q. Li, X. Cai, P. Zhou, Z. Wu, B. Wang, W. Ma, S. Fu, Injectable hydrogels as drug delivery platform for in-situ treatment of malignant tumor, J. Drug Deliv. Sci. Technol. 76 (2022) 103817.
[12] M.M.H. Rumon, A.A. Akib, F. Sultana, M. Moniruzzaman, M.S. Niloy, M.S. Shakil, C.K. Roy, Self-healing hydrogels: development, biomedical applications, and challenges, Polymers 14 (21) (2022) 4539.
[13] J. Xu, Y. Liu, S.-h. Hsu, Hydrogels based on schiff base linkages for biomedical applications, Molecules 24 (16) (2019) 3005.
[14] Y. Xu, Y. Li, Q. Chen, L. Fu, L. Tao, Y. Wei, Injectable and self-healing chitosan hydrogel based on imine bonds: design and therapeutic applications, Int. J. Mol. Sci. 19 (8) (2018) 2198.
[15] Y. Li, X. Wang, Y. Wei, L. Tao, Chitosan-based self-healing hydrogel for bioapplications, Chin. Chem. Lett. 28 (11) (2017) 2053–2057.
[16] Z. Shariatinia, Carboxymethyl chitosan: properties and biomedical applications, Int. J. Biol. Macromol. 120 (2018) 1406–1419.
[17] T.-C. Tseng, L. Tao, F.-Y. Hsieh, Y. Wei, I.-M. Chiu, S.-h. Hsu, An injectable, self-healing hydrogel to repair the central nervous system, Adv. Mater. 27 (23) (2015) 3518–3524.
[18] T.-W. Lin, S.-h. Hsu, Self-healing hydrogels and cryogels from biodegradable polyurethane nanoparticle crosslinked chitosan, Adv. Sci. 7 (3) (2020) 1901388.
[19] C.-W. Wong, F.W. Pratiwi, P. Chen, C.-Y. Mou, S.-h. Hsu, Revealing the phagosomal pH regulation and inflammation of macrophages after endocytosing polyurethane nanoparticles by A ratiometric pH nanosensor, Advanced Biology 5 (1) (2021) 2000200.
[20] J. Xu, C.-H. Tai, T.-Y. Chen, S.-h. Hsu, An anti-inflammatory electroconductive hydrogel with self-healing property for the treatment of Parkinson's disease, Chem. Eng. J. 446 (2022) 137180.
[21] Y. Lang, N. Gao, Z. Zang, X. Meng, Y. Lin, S. Yang, Y. Yang, Z. Jin, B. Li, Classification and antioxidant assays of polyphenols: a review, Journal of Future Foods 4 (3) (2024) 193–204.

[22] A. Singh, P. Tripathi, A.K. Yadawa, S. Singh, Promising polyphenols in parkinson's disease therapeutics, Neurochem. Res. 45 (8) (2020) 1731–1745.
[23] M. Caruana, R. Cauchi, N. Vassallo, Putative role of red wine polyphenols against brain pathology in alzheimer's and Parkinson's disease, Front. Nutr. 3 (2016).
[24] H. Badoni, S. Painuli, S. Panwar, P. Sharma, P. Semwal, Screening of anti-parkinson activity of tannic acid via antioxidant and neuroprotection in Wistar rats, Brain Disorders 13 (2024) 100109.
[25] S. Azimullah, M.F. Meeran, K. Ayoob, S. Arunachalam, S. Ojha, R. Beiram, Tannic acid mitigates rotenone-induced dopaminergic neurodegeneration by inhibiting inflammation, oxidative stress, apoptosis, and glutamate toxicity in rats, Int. J. Mol. Sci. 24 (12) (2023).
[26] M.F.B. Gerzson, N.P. Bona, M.S.P. Soares, F.C. Teixeira, F.L. Rahmeier, F. B. Carvalho, M. da Cruz Fernandes, G. Onzi, G. Lenz, R.A. Gonçales, R. M. Spanevello, F.M. Stefanello, Tannic acid ameliorates STZ-induced alzheimer's disease-like impairment of memory, neuroinflammation, neuronal death and modulates akt expression, Neurotox. Res. 37 (4) (2020) 1009–1017.
[27] J. Xu, T.-Y. Chen, C.-H. Tai, S.-h. Hsu, Bioactive self-healing hydrogel based on tannic acid modified gold nano-crosslinker as an injectable brain implant for treating Parkinson's disease, Biomater. Res. 27 (1) (2023) 8.
[28] E. Hamdi, S. Hidouri, A.-B. Muniz-Gonzalez, M. Kechnebbou, S. Amara, Harnessing silica nanoparticles grafted with ascorbic acid to alleviate oxidative stress and impaired brain activity in rats, Nano TransMed 4 (2025) 100074.
[29] J.-M. Lin, C.-Y. Chen, Y.-W. Tsai, Y.-S. Huang, Coherent X-ray scattering for microanalysis at Taiwan photon source, Microsc. Microanal. 24 (S2) (2018) 262–263.
[30] A. Guinier, G. Fournet, C.B. Walker, G.H. Vineyard, Small-angle scattering of X-rays, in: A. Guinier, G. Fournet (Eds.), Acta Crystallogr. 9 (3) (1956) 326, 326.
[31] J.K. Percus, G.J. Yevick, Analysis of classical statistical mechanics by means of collective coordinates, Phys. Rev. 110 (1) (1958) 1–13.
[32] B. Hammouda, D.L. Ho, Insight into chain dimensions in PEO/water solutions, J. Polym. Sci. B Polym. Phys. 45 (16) (2007) 2196–2200.
[33] J. Xu, P. Dai, C. Zhang, N. Dong, C. Li, C. Tang, Z. Jin, S.-H. Lin, L. Ye, T. Sun, Y. Jin, F. Wu, L. Luo, P. Wu, S. Li, X. Li, S.-h. Hsu, D. Jiang, Z. Wang, Injectable hierarchical bioactive hydrogels with fibroblast growth factor 21/Edaravone/Caffeic acid asynchronous delivery for treating Parkinson's Disease, Adv. Sci. 12 (4) (2025) 2412020.
[34] T.-Y. Chen, J. Xu, C.-H. Tai, T.-K. Wen, S.-h. Hsu, Biodegradable, electroconductive self-healing hydrogel based on polydopamine-coated polyurethane nano-crosslinker for Parkinson's disease therapy, Biomaterials 320 (2025) 123268.
[35] J. Li, M. Darabi, J. Gu, J. Shi, J. Xue, L. Huang, Y. Liu, L. Zhang, N. Liu, W. Zhong, L. Zhang, M. Xing, L. Zhang, A drug delivery hydrogel system based on activin B for Parkinson's disease, Biomaterials 102 (2016) 72–86.
[36] G. Paxinos, C.R. Watson, P.C. Emson, AChE-stained horizontal sections of the rat brain in stereotaxic coordinates, J. Neurosci. Methods 3 (2) (1980) 129–149.
[37] J.L. Hudson, C.G. van Horne, I. Strömberg, S. Brock, J. Clayton, J. Masserano, B. J. Hoffer, G.A. Gerhardt, Correlation of apomorphine-and amphetamine-induced turning with nigrostriatal dopamine content in unilateral 6-hydroxydopamine lesioned rats, Brain Res. 626 (1–2) (1993) 167–174.
[38] G. Paxinos, C. Watson, The Rat Brain in Stereotaxic Coordinates: Hard Cover Edition, Elsevier, 2006.
[39] H. Heberle, G.V. Meirelles, F.R. da Silva, G.P. Telles, R. Minghim, InteractiVenn: a web-based tool for the analysis of sets through Venn diagrams, BMC Bioinf. 16 (1) (2015) 169.
[40] J. Su, M. Huo, F. Xu, L. Ding, Molecular mechanism of lycorine in the treatment of glioblastoma based on network pharmacology and molecular docking, N. Schmied. Arch. Pharmacol. 397 (3) (2024) 1551–1559.
[41] P. Orlowski, E. Tomaszewska, K. Ranoszek-Soliwoda, M. Gniadek, O. Labedz, T. Malewski, J. Nowakowska, G. Chodaczek, G. Celichowski, J. Grobelny, M. Krzyzowska, Tannic acid-modified silver and gold nanoparticles as novel stimulators of dendritic cells activation, Front. Immunol. 9 (2018).
[42] Y.-P. Chen, S.-h. Hsu, Preparation and characterization of novel water-based biodegradable polyurethane nanoparticles encapsulating superparamagnetic iron oxide and hydrophobic drugs, J. Mater. Chem. B 2 (21) (2014) 3391–3401.
[43] N. Sp, D.Y. Kang, D.H. Kim, J.-S. Yoo, E.S. Jo, A. Rugamba, K.-J. Jang, Y.M. Yang, Tannic acid inhibits non-small cell lung cancer (NSCLC) stemness by inducing G0/G1 cell cycle arrest and intrinsic apoptosis, Anticancer Res. 40 (6) (2020) 3209–3220.
[44] S.A. Abouelmagd, F. Meng, B.-K. Kim, H. Hyun, Y. Yeo, Tannic acid-mediated surface functionalization of polymeric nanoparticles, ACS Biomater. Sci. Eng. 2 (12) (2016) 2294–2303.
[45] J. Ilavsky, P.R. Jemian, A.J. Allen, F. Zhang, L.E. Levine, G.G. Long, Ultra-small-angle X-ray scattering at the advanced photon source, Applied Crystallography 42 (3) (2009) 469–479.
[46] S.-H. Lin, C.M. Papadakis, J.-J. Kang, J.-M. Lin, S.-h. Hsu, Injectable phenolic-chitosan self-healing hydrogel with hierarchical micelle architectures and fast adhesiveness, Chem. Mater. 33 (11) (2021) 3945–3958.
[47] A. Guinier, G. Fournet, C.B. Walker, K.L. Yudowitch, Small-Angle Scattering of X-rays, Wiley New York, 1955.
[48] T. Schindler, M. Schmiele, T. Schmutzler, T. Kassar, D. Segets, W. Peukert, A. Radulescu, A. Kriele, R. Gilles, T. Unruh, A combined SAXS/SANS study for the in situ characterization of ligand shells on small nanoparticles: the case of ZnO, Langmuir 31 (37) (2015) 10130–10136.
[49] X. Zha, A. Travesset, The hard sphere diameter of nanocrystals (nanoparticles), J. Chem. Phys. 152 (9) (2020).
[50] T. Schindler, J. Walter, W. Peukert, D. Segets, T. Unruh, In situ study on the evolution of multimodal particle size distributions of ZnO quantum dots: some general rules for the occurrence of multimodalities, J. Phys. Chem. B 119 (49) (2015) 15370–15380.
[51] A. Mishra, B.P.D. Purkayastha, J.K. Roy, V.K. Aswal, P. Maiti, Tunable properties of self-assembled polyurethane using two-dimensional nanoparticles: potential nano-biohybrid, Macromolecules 43 (23) (2010) 9928–9936.
[52] A. Mishra, S.K. Singh, D. Dash, V.K. Aswal, B. Maiti, M. Misra, P. Maiti, Self-assembled aliphatic chain extended polyurethane nanobiohybrids: emerging hemocompatible biomaterials for sustained drug delivery, Acta Biomater. 10 (5) (2014) 2133–2146.
[53] E.F. Dudás, A. Bodor, Quantitative, diffusion NMR based analytical tool to distinguish folded, disordered, and denatured biomolecules, Anal. Chem. 91 (8) (2019) 4929–4933.
[54] M. Chen, T. Runge, L. Wang, R. Li, J. Feng, X.-L. Shu, Q.-S. Shi, Hydrogen bonding impact on chitosan plasticization, Carbohydr. Polym. 200 (2018) 115–121.
[55] S. Guo, Y. Ren, R. Chang, Y. He, D. Zhang, F. Guan, M. Yao, Injectable self-healing adhesive chitosan hydrogel with antioxidative, antibacterial, and hemostatic activities for rapid hemostasis and skin wound healing, ACS Appl. Mater. Interfaces 14 (30) (2022) 34455–34469.
[56] L.-J. Huang, S.-H. Lin, T.-Y. Chen, S.-h. Hsu, Chitosan catechol-tannic acid composite hydrogel and cryogel with antimicrobial and hemostatic properties, Int. J. Biol. Macromol. 270 (2024) 132174.
[57] İ. Gülçin, Z. Huyut, M. Elmastaş, H.Y. Aboul-Enein, Radical scavenging and antioxidant activity of tannic acid, Arab. J. Chem. 3 (1) (2010) 43–53.
[58] Y. Wu, L. Zhong, Z. Yu, J. Qi, Anti-neuroinflammatory effects of tannic acid against lipopolysaccharide-induced BV2 microglial cells via inhibition of NF-κB activation, Drug Dev. Res. 80 (2) (2019) 262–268.
[59] S. Mishra, M. Botlagunta, S. Rajasekaran, Arsenic-induced inflammatory response via ROS-dependent activation of ERK/NF-kB signaling pathways: protective role of natural polyphenol tannic acid, J. Appl. Toxicol. 45 (5) (2025) 795–807.
[60] Y. Xue, M. Li, Y. Xue, W. Jin, X. Han, J. Zhang, X. Chu, Z. Li, L. Chu, Mechanisms underlying the protective effect of tannic acid against arsenic trioxide-induced cardiotoxicity in rats: potential involvement of mitochondrial apoptosis, Mol. Med. Rep. 22 (6) (2020) 4663–4674.
[61] W. Liao, Z. Liu, T. Zhang, S. Sun, J. ye, Z. Li, L. Mao, J. Ren, Enhancement of anti-inflammatory properties of nobiletin in macrophages by a nano-emulsion preparation, J. Agric. Food Chem. 66 (1) (2018) 91–98.
[62] P. Chakraborty, P. Dipankar, S.P. Dash, Priya, S. Srivastava, R. Dhyani, N. K. Navani, D. Sharma, P.P. Sarangi, Electrostatic surface potential of macrophages correlates with their functional phenotype, Inflammation 43 (2) (2020) 641–650.
[63] N. Xu, Y. Gao, Z. Li, Y. Chen, M. Liu, J. Jia, R. Zeng, G. Luo, J. Li, Y. Yu, Immunoregulatory hydrogel decorated with tannic Acid/ferric ion accelerates diabetic wound healing via regulating macrophage polarization, Chem. Eng. J. 466 (2023) 143173.
[64] F. Blandini, G. Levandis, E. Bazzini, G. Nappi, M.T. Armentero, Time-course of nigrostriatal damage, basal ganglia metabolic changes and behavioural alterations following intrastriatal injection of 6-hydroxydopamine in the rat: new clues from an old model, Eur. J. Neurosci. 25 (2) (2007) 397–405.
[65] Y.-Y. Wang, Y. Wang, H.-F. Jiang, J.-H. Liu, J. Jia, K. Wang, F. Zhao, M.-H. Luo, M.-M. Luo, X.-M. Wang, Impaired glutamatergic projection from the motor cortex to the subthalamic nucleus in 6-hydroxydopamine-lesioned hemi-parkinsonian rats, Exp. Neurol. 300 (2018) 135–148.
[66] M.-K. Pan, C.-H. Tai, W.-C. Liu, J.-C. Pei, W.-S. Lai, C.-C. Kuo, Deranged NMDAergic cortico-subthalamic transmission underlies parkinsonian motor deficits, J. Clin. Investig. 124 (10) (2014) 4629–4641.
[67] M. Jakobs, A. Fomenko, A.M. Lozano, K.L. Kiening, Cellular, molecular, and clinical mechanisms of action of deep brain stimulation—a systematic review on established indications and outlook on future developments, EMBO Mol. Med. 11 (4) (2019) e9575.
[68] K. Kaczyńska, K. Andrzejewski, Chapter 40 - 6-hydroxydopamine-induced model of Parkinson's disease, in: C.R. Martin, V.R. Preedy (Eds.), Genetics, Neurology, Behavior, and Diet in Parkinson's disease, Academic Press, 2020, pp. 627–642.
[69] S.S. Singh, S.N. Rai, H. Birla, W. Zahra, A.S. Rathore, S.P. Singh, NF-κB-Mediated neuroinflammation in parkinson's disease and potential therapeutic effect of polyphenols, Neurotox. Res. 37 (3) (2020) 491–507.
[70] J. Xue, Y. Liu, M.A. Darabi, G. Tu, L. Huang, L. Ying, B. Xiao, Y. Wu, M. Xing, L. Zhang, L. Zhang, An injectable conductive Gelatin-PANI hydrogel system serves as a promising carrier to deliver BMSCs for Parkinson's disease treatment, Mater. Sci. Eng. C 100 (2019) 584–597.
[71] H.-Y. Yang, J. Wu, H. Lu, M.-L. Cheng, B.-H. Wang, H.-L. Zhu, L. Liu, M. Xie, Emodin suppresses oxaliplatin-induced neuropathic pain by inhibiting COX2/NF-κB mediated spinal inflammation, J. Biochem. Mol. Toxicol. 37 (1) (2023) e23229.
[72] S. Giridharan, M. Srinivasan, Mechanisms of NF-κB p65 and strategies for therapeutic manipulation, J. Inflamm. Res. (2018) 407–419.

[73] W. Zha, Q. Zhao, Y. Xiao, Y. Gan, J. Wei, M. Yu, Y. Xu, Q. Xu, S. Wu, W. Yu, Mitochonic acid 5 rescues cardiomyocytes from doxorubicin-induced toxicity via repressing the TNF-α/NF-κB/NLRP3-mediated pyroptosis, Int. Immunopharmacol. 123 (2023) 110736.
[74] F. Yulak, M. Ergul, Tannic acid protects neuroblastoma cells against hydrogen peroxide – triggered oxidative stress by suppressing oxidative stress and apoptosis, Brain Res. 1844 (2024) 149175.
[75] J. García-Revilla, R. Ruiz, A.M. Espinosa-Oliva, M. Santiago, I. García-Domínguez, L. Camprubí-Ferrer, S. Bachiller, T. Deierborg, B. Joseph, R.M. de Pablos, J. A. Rodríguez-Gómez, J.L. Venero, Dopaminergic neurons lacking Caspase-3 avoid apoptosis but undergo necrosis after MPTP treatment inducing a Galectin-3-dependent selective microglial phagocytic response, Cell Death Dis. 15 (8) (2024) 625.
[76] Y. Liu, Y. Guo, S. An, Y. Kuang, X. He, H. Ma, J. Li, J. Lv, N. Zhang, C. Jiang, Targeting Caspase-3 as dual therapeutic benefits by RNAi facilitating brain-targeted nanoparticles in a rat model of parkinson's disease, PLoS One 8 (5) (2013) e62905.